Article

Cell Stem Cell

A Homeostatic Arid1a-Dependent Permissive Chromatin State Licenses Hepatocyte Responsiveness to Liver-Injury-Associated YAP Signaling

Graphical Abstract

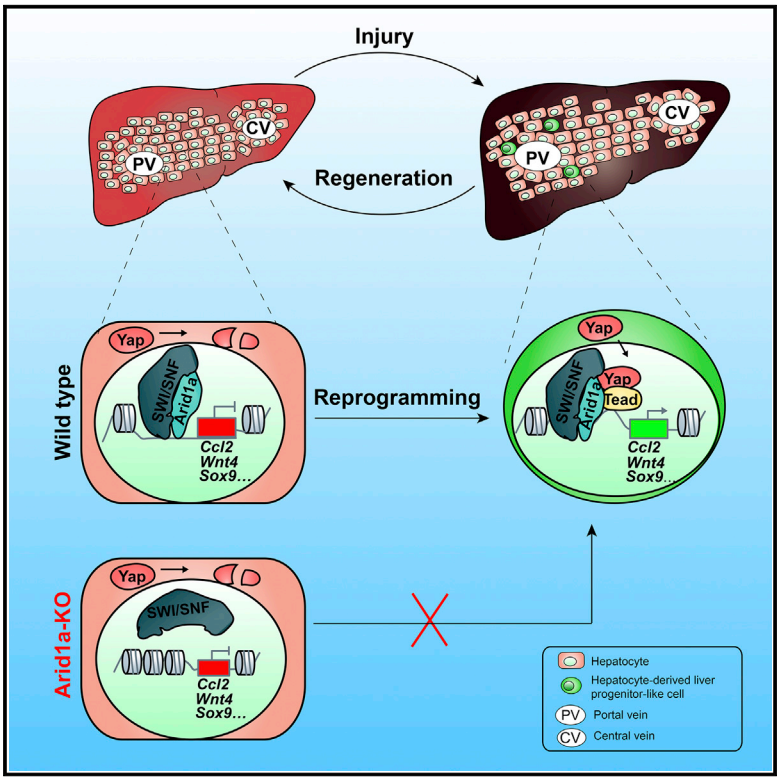

Authors

Weiping Li, Liguang Yang, Qiang He, ..., Hong Li, Yixue Li, Lijian Hui

Correspondence

lihong01@sibs.ac.cn (H.L.),
yxli@sibs.ac.cn (Y.L.),
ljhui@sibcb.ac.cn (L.H.)

In Brief

In vivo cellular reprogramming after injury can regenerate injured tissue and restore function. Li et al. show that Arid1a regulates liver regeneration by promoting a permissive chromatin state in hepatocytes, which renders them competent to respond to injury-associated regenerative signals and facilitates expression of liver-progenitor-like cell genes.

Highlights

- Arid1a expression in hepatocytes promotes liver regeneration after periportal injuries
- Arid1a endows a permissive chromatin state to liver-progenitor-like cell-enriched genes
- Arid1a-dependent permissive chromatin defines responsiveness to regenerative signals

Data Resources

GSE111502

Li et al., 2019, Cell Stem Cell *25*, 54–68
July 3, 2019
https://doi.org/10.1016/j.stem.2019.06.008

CellPress

CellPress

Cell Stem Cell
Article

A Homeostatic Arid1a-Dependent Permissive Chromatin State Licenses Hepatocyte Responsiveness to Liver-Injury-Associated YAP Signaling

Weiping Li,[1,11] Liguang Yang,[2,11] Qiang He,[1,11] Chaobo Hu,[1] Linying Zhu,[1] Xiaolong Ma,[1] Xueyan Ma,[1] Shujie Bao,[1] Lu Li,[1] Yingying Chen,[1] Xing Deng,[6] Xin Zhang,[6] Jin Cen,[1] Lei Zhang,[1] Zhong Wang,[7] Wei-Fen Xie,[6] Hong Li,[2,*] Yixue Li,[2,3,4,5,*] and Lijian Hui[1,8,9,10,12,*]

[1]State Key Laboratory of Cell Biology, CAS Center for Excellence in Molecular Cell Science, Shanghai Institute of Biochemistry and Cell Biology, Chinese Academy of Sciences, University of Chinese Academy of Sciences, Shanghai 200031, China
[2]CAS Key Laboratory of Computational Biology, CAS-MPG Partner Institute for Computational Biology, Shanghai Institute of Nutrition and Health, Shanghai Institutes for Biological Sciences, University of Chinese Academy of Sciences, Chinese Academy of Sciences, Shanghai 200031, China
[3]School of Life Sciences and Biotechnology, Shanghai Jiao Tong University, Shanghai 200240, China
[4]Collaborative Innovation Center of Genetics and Development, Fudan University, Shanghai 200433, China
[5]Shanghai Center for Bioinformation Technology, Shanghai Academy of Science and Technology, Shanghai 201203, China
[6]Department of Gastroenterology, Changzheng Hospital, Second Military Medical University, Shanghai 200003, China
[7]Department of Cardiac Surgery, Cardiovascular Research Center, University of Michigan, Michigan 48109, USA
[8]Institute for Stem Cell and Regeneration, Chinese Academy of Sciences, Beijing 100101, China
[9]Bio-Research Innovation Center, Shanghai Institute of Biochemistry and Cell Biology, Chinese Academy of Sciences, Suzhou 215121, China
[10]School of Life Science and Technology, ShanghaiTech University, Shanghai 201210, China
[11]These authors contributed equally
[12]Lead Contact
*Correspondence: lihong01@sibs.ac.cn (H.L.), yxli@sibs.ac.cn (Y.L.), ljhui@sibcb.ac.cn (L.H.)
https://doi.org/10.1016/j.stem.2019.06.008

SUMMARY

Following injury, differentiated epithelial cells can serve as a stem cell-independent source for tissue regeneration by undergoing reprogramming into other cell types. The intrinsic molecular basis underlying plasticity of differentiated cells remains largely unaddressed. Here we show that Arid1a, a key component of the SWI/SNF chromatin remodeling complex, controls liver regeneration and gene expression associated with emergence of injury-induced liver-progenitor-like cells (LPLCs). Hepatocyte-specific Arid1a ablation reduces LPLC gene expression in several models of periportal liver injury and impairs liver regeneration, leading to organ dysfunction. Arid1a establishes a permissive chromatin state at LPLC-enriched genes during homeostasis, suggesting it endows hepatocytes with competence to respond to injury-induced signals. Consistently, Arid1a facilitates binding of YAP, a critical regeneration signaling pathway, to LPLC-enriched genes, and Arid1a deletion prevents their YAP-associated induction following injury. Together, these findings provide a framework for studying the contributions of injury-induced LPLCs to periportal liver regeneration.

INTRODUCTION

Mammalian organs comprise an extraordinary diversity of cell and tissue types. In injured mammalian epithelial tissues, such as the skin and intestine, adult stem cells have been proposed as the cell source in maintaining tissue homeostasis (Blanpain and Fuchs, 2014). However, recent studies uncover that differentiated cells can replenish injured tissues by dedifferentiation or transdifferentiation into other types of cells, as demonstrated in the lung alveolus (Jain et al., 2015), gastric gland (Stange et al., 2013), intestinal crypt (Tetteh et al., 2016), pancreatic islet (Kopp et al., 2016), and liver parenchyma (Kopp et al., 2016). Due to the plenty of resident differentiated cells and their reprogramming after injuries, potential therapeutic approaches have been proposed to harness the plasticity of differentiated cells for *in situ* tissue repair and regeneration. Apparently, a better understanding of the underlying mechanism of injury-induced cell identity conversion *in vivo* will facilitate the development of cell-plasticity-based regenerative therapies.

Cell identity conversion is mainly related to transcriptional regulation by transcription factors, cell signaling, and epigenetic modifications (Apostolou and Hochedlinger, 2013). Previous studies of *in vivo* cell reprogramming have uncovered important roles of transcription factors and cell signaling in cell plasticity regulation (Wells and Watt, 2018). For example, inactivation of Fbw7, a substrate-recognizing component of SCF-type E3 ubiquitin ligase, induces pancreatic ductal cells to α, δ, and β cells by stabilizing the transcription factor Neurog3, a known regulator of endocrine cell differentiation (Sancho et al., 2014). The interaction between transcription factors and extracellular signals in reprogramming has been exemplified by a recent study showing that the deficiency in formation of intrahepatic bile ducts caused severe cholestatic injury and triggered hepatocyte to biliary cell conversion via the TGFβ-Smad pathway (Schaub et al., 2018).

Epigenetic modifications, including DNA methylation, histone modifications, and chromatin remodeling, are another layer of

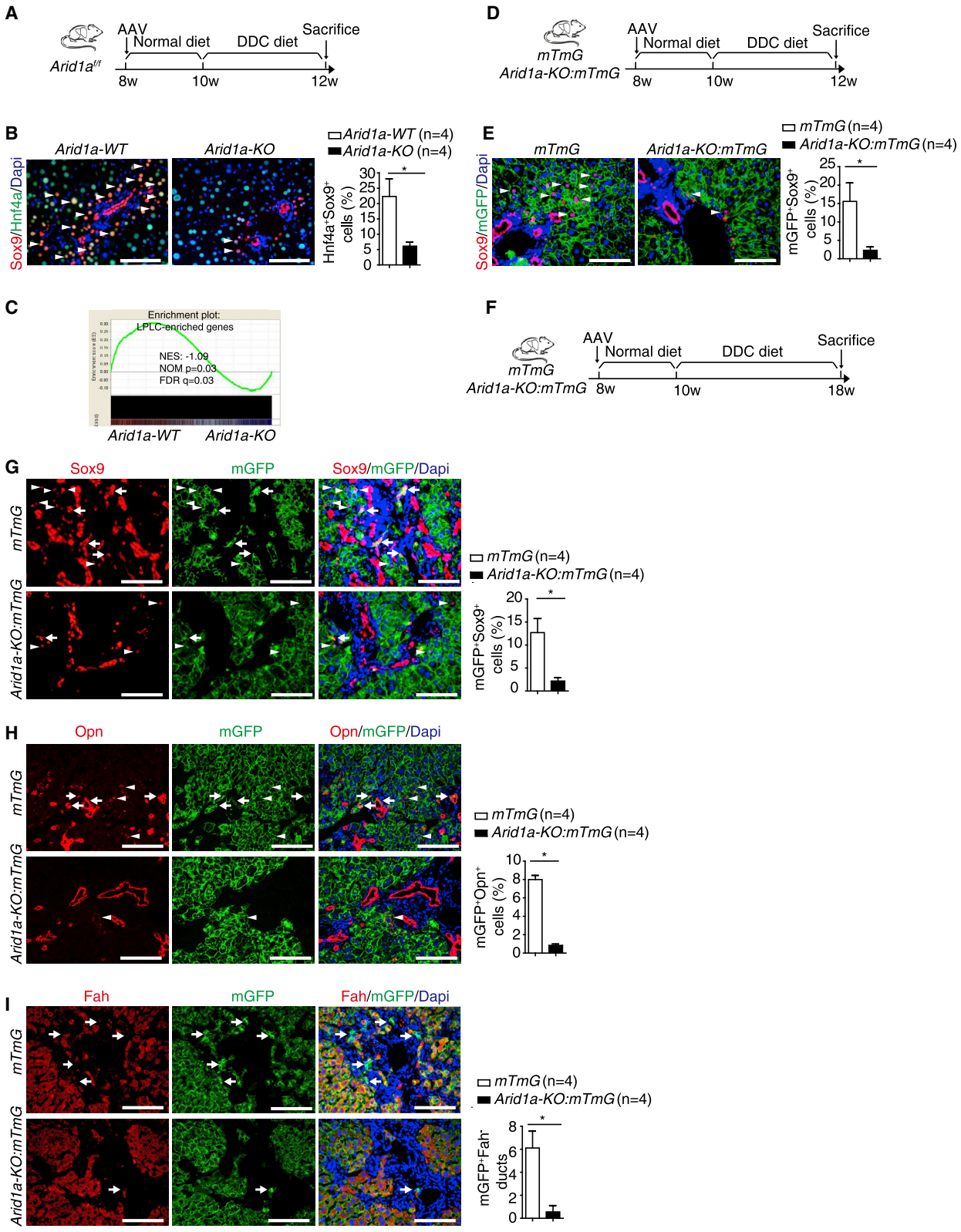

Figure 1. Arid1a Is Required for Hepatocyte to Liver-Progenitor-Like Cell Formation in Periportal Injury

(A) Experimental design of DDC-induced hepatocyte to LPLC formation. *Arid1a* was deleted via tail vein injection of AAV-Cre in *Arid1a*$^{f/f}$ mice (*Arid1a-KO*). *Arid1a*$^{f/f}$ mice treated with AAV-GFP (*Arid1a-WT*) were used as control.

(legend continued on next page)

regulation of transcription. The importance of epigenetic regulations is well demonstrated in somatic cell identity conversion *in vitro* (Apostolou and Hochedlinger, 2013; Nashun et al., 2015). For example, the SWI/SNF chromatin remodeling complex, which is recruited by Oct4, remodels the chromatin structure and facilitates binding of other transcription factors for iPSC induction (Singhal et al., 2010). Interestingly, epigenetic modifications of somatic cells mainly serve as a barrier during *in vitro* cell identity conversion. Inactivation of histone methyltransferases G9a or Setdb1 increases the accessibility of H3K9-methylation-markered heterochromatic regions to transcription factors and results in more efficient iPSC induction (Chen et al., 2013; Soufi et al., 2012). We also showed that Baf60b mediates a chromatin remodeling checkpoint that activates ATM/p53-dependent lineage restriction in hepatic reprogramming (Ji et al., 2017; Zaret, 2017). However, the role of epigenetic regulation remains yet unclear in reprogramming *in vivo*. Cell identity conversion *in vitro* and *in vivo* is different in that *in vivo* conversion happens in the microenvironment rich in extracellular signals, which needs to be properly integrated with the epigenetic modifications.

To study the intrinsic epigenetic regulation of the plasticity of differentiated cells in epithelia organs, we investigated conversion from hepatocytes to liver-progenitor-like cells (LPLCs) and its significance for regeneration in the injured liver. In various types of periportal liver injuries, differentiated hepatocytes were previously found to be plastic and convert to LPLCs via a bi-phenotypical state, expressing both hepatocyte genes and liver progenitor genes (Tanimizu et al., 2014; Tarlow et al., 2014b; Yanger et al., 2013). In this study, we uncovered that the chromatin status of LPLC-enriched genes is permissive in hepatocytes under the resting condition. The permissive chromatin status is facilitated by Arid1a-mediated chromatin opening. Arid1a-dependent permissive chromatin endows hepatocytes with the competence to respond to the Hippo/Yap signal, which activates the expression of LPLC-enriched genes during periportal liver injury. Notably, Arid1a ablation results in defected LPLC formation, impaired regeneration, and liver dysfunctions. Our study indicates an intrinsic epigenetic basis underlying hepatocyte competence in responding to regenerative signals in injury, which may help us to understand cell plasticity in other epithelial tissues.

RESULTS

Identification of Epigenetic Factors Involved in Injury-Induced Liver-Progenitor-Like Cells

To identify epigenetic factors controlling injury-induced LPLCs, we retrieved published RNA-seq data in LPLCs (Tarlow et al., 2014b) and analyzed them with available Cistrome ChIP-seq data of epigenetic factors related to livers and hepatocytes (Table S1 and STAR Methods). Among the 12 epigenetic factors analyzed, Arid1a was the top one, showing significant binding to genes whose expression levels were altered between hepatocytes and LPLCs (Table S2). Importantly, LPLC conversion-related pathways were found in genes bound by Arid1a (Table S3). Arid1a is the core regulatory component of the SWI/SNF complex (Lessard and Crabtree, 2010), an ATP-dependent chromatin remodeling complex that plays important roles in induced pluripotency and cell lineage commitment (Eroglu et al., 2014; Koche et al., 2011; Singhal et al., 2010; Skibinski et al., 2014). Interestingly, Arid1a is one of the most frequently mutated genes in human liver tumorigenesis, a process usually related to impaired regeneration (Guichard et al., 2012). We decided to focus on Arid1a in this study.

Arid1a Facilitates Liver-Progenitor-Like Cell Formation in Periportal Liver Injury

To specifically characterize the role of Arid1a in periportal-injury-induced LPLCs, we delivered adeno-associated viruses carrying Cre recombinase under the regulation of the *thyroid hormone-binding globulin* promoter (AAV-Cre) into *Arid1a*$^{f/f}$ adult mice (*Arid1a-WT*). AAV-Cre treatment specifically and efficiently deleted *Arid1a* in hepatocytes (*Arid1a-KO*), which showed normal liver morphology and functions under the resting condition (Figures S1A–S1D). These mice were subjected to the 3,5-diethoxycarbonyl-1,4-dihydrocollidine (DDC) diet to induce hepatocyte to LPLC formation (Figure 1A).

DDC treatment caused periportal hepatic toxicity and ductular reaction in both *Arid1a-WT* and *Arid1a-KO* mice (Figure 1B and Figures S1E–S1I). DDC treatment for 2 weeks induced remarkable LPLC formation in Arid1a-WT mice, which retained typical hepatocyte morphology and expressed both hepatocyte transcription factor Hnf4a and liver progenitor markers Sox9, Opn, and CD24 (Tanimizu et al., 2014, 2017; Tarlow et al., 2014b; Yanger et al., 2013) (Figure 1B and Figure S1J). While LPLCs were not detectable under the resting condition (Figure S1K), they were readily identified as early as 3 days after DDC injury by Sox9, Opn, and CD24 staining (Figure S1L). By contrast, the number of Hnf4a$^+$Sox9$^+$ and Hnf4a$^+$Opn$^+$ and Hnf4a$^+$CD24$^+$ cells was significantly reduced in *Arid1a-KO* livers after DDC treatment for 3 days or 2 weeks (Figure 1B, Figure S1J, and Figure S1L). Gene expression profiling analysis also showed that mRNA levels of genes enriched in LPLCs (hereafter called LPLC-enriched genes, see STAR Methods) (Tarlow et al., 2014b) were also suppressed in *Arid1a-KO* mice (Figure 1C),

(B) Co-staining of hepatocyte marker Hnf4a and progenitor cell marker Sox9 in *Arid1a-WT* and *Arid1a-KO* livers after 2 weeks of DDC treatment. Arrowheads indicated Hnf4a$^+$Sox9$^+$ LPLCs. The ratio of Hnf4a$^+$Sox9$^+$ hepatocytes to Hnf4a$^+$ hepatocytes per periportal field of view was shown.

(C) GSEA analysis of the expression of LPLC-enriched genes in *Arid1a-WT* and *Arid1a-KO* livers after 2 weeks of DDC treatment.

(D) Schematic view of hepatocyte labeling using *mTmG* mice. AAV-Cre treatment converted mTomato$^+$ hepatocytes to mGFP$^+$ cells, leaving other non-hepatocytes as mTomato$^+$.

(E) LPLCs were detected by co-staining of GFP and Sox9 in *mTmG* and *Arid1a-KO:mTmG* livers after 2 weeks of DDC treatment. Arrowheads indicated mGFP$^+$Sox9$^+$ cells. The ratio of mGFP$^+$Sox9$^+$ hepatocytes to mGFP$^+$ hepatocytes per periportal field of view was shown.

(F–I) Analyses of LPLC formation in *mTmG* and *Arid1a-KO:mTmG* livers after DDC treatment for 8 weeks is shown in (F). Co-staining of GFP and Sox9 (G), GFP and Opn (H), and GFP and Fah (I) in *mTmG* and *Arid1a-KO:mTmG* livers is also shown. Arrowheads indicate mGFP$^+$Sox9$^+$ and mGFP$^+$Opn$^+$ LPLCs, and arrows indicate bile duct-like cells. Quantification of mGFP$^+$Sox9$^+$ and mGFP$^+$Opn$^+$ hepatocytes is shown as the ratio to mGFP$^+$ hepatocytes per periportal field of view (G and H). The number of mGFP$^+$Fah$^-$ ducts was quantified per periportal field of view (I).

n represents the number of animals for analyses. Data were presented as mean ± SEM; *$p < 0.05$, t test; scale bar represents 100 μm. See also Figures S1 and S2.

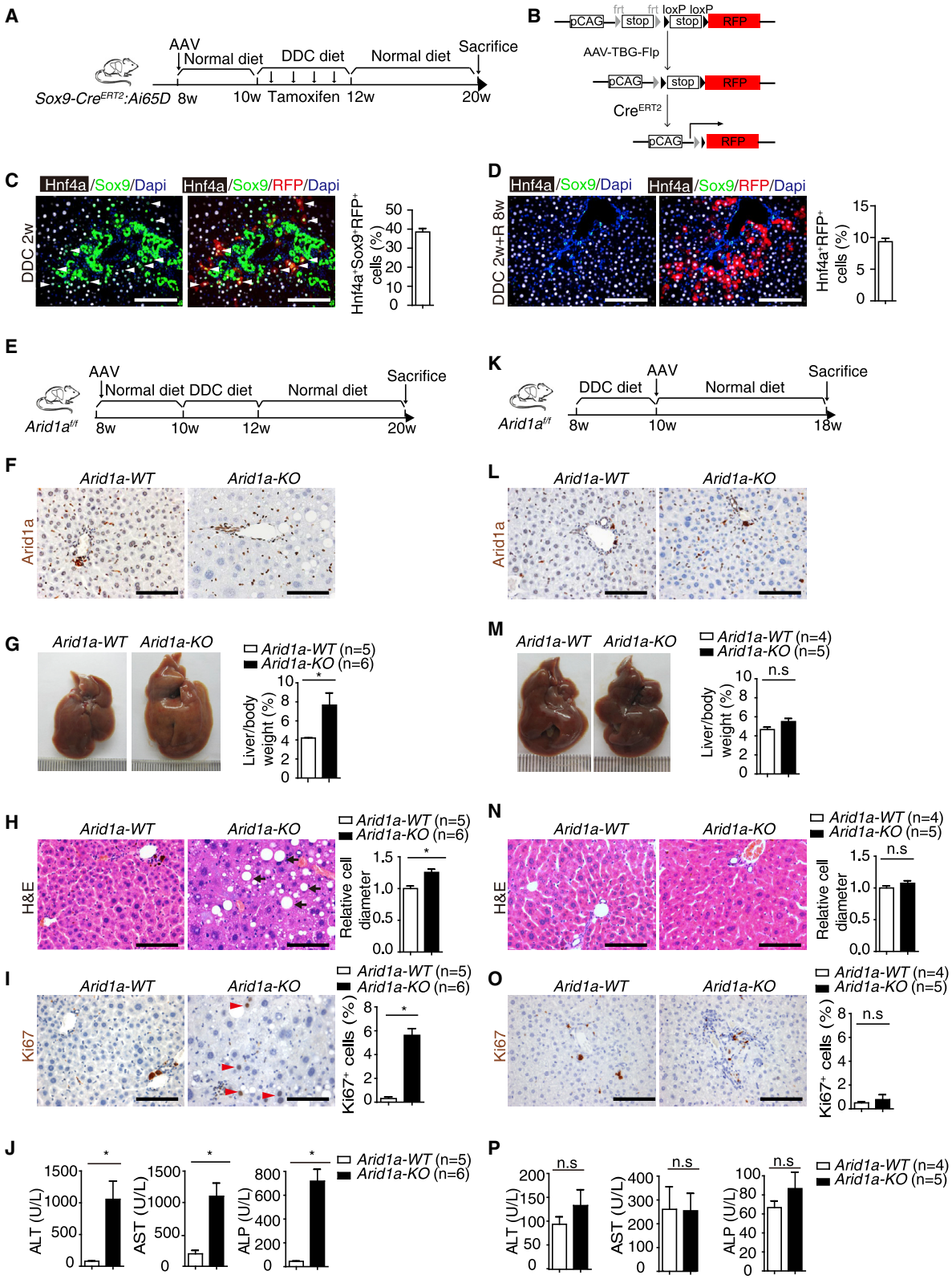

Figure 2. Arid1a-Dependent Liver-Progenitor-Like Cell Formation Contributes to Periportal-Injury-Induced Liver Regeneration

(A) Experimental design of lineage tracing of LPLCs in liver injury and recovery.

(B) DDC injury-induced Hnf4a^{+}Sox9^{+} LPLCs were labeled by *Sox9-Cre^{ERT2}:Ai65D* reporter mice.

(legend continued on next page)

as exemplified by critical genes in Hippo/Yap and Notch pathways (Figure S1M). Notably, *Arid1a-WT* and *Arid1a-KO* livers showed comparable cell proliferation and cell death upon DDC injury (Figures S1N–S1P), further supporting a role of Arid1a in injury-induced LPLCs.

Next, we traced hepatocytes in DDC-induced injury using *Rosa26-loxP-mTomato-stop-loxP-mGFP* (*mTmG*) reporter mice (Figure 1D). AAV-Cre treatment efficiently converted mTomato$^+$ hepatocytes to mGFP$^+$ cells, leaving other non-hepatocytes as mTomato$^+$ under the resting condition (Figure S2A). In these mice, DDC-induced LPLCs were all positive for mGFP (Figure S2B), confirming their origination from mature hepatocytes. The number of LPLCs (mGFP$^+$Sox9$^+$) was markedly reduced in *Arid1a-KO:mTmG* mice (Figure 1E). It has been reported that LPLCs could give rise to bile-duct-like cells after extended injury (Figure 1F). Indeed, mGFP$^+$ cells, which displayed ductal-like morphology with increased expression of progenitor markers Sox9 and Opn (Figures 1G and 1H) and diminished expression of the mature hepatocyte gene Fah (Figure 1I), were detectable in the periportal area of *mTmG* mice after extended DDC treatment for 8 weeks. Moreover, we found integration of mGFP$^+$ cells into the bile ducts as shown by CK19 staining (Figure S2C), supporting a duct fate of LPLCs (Tanimizu et al., 2014; Tarlow et al., 2014b; Yanger et al., 2013). By contrast, *Arid1a-KO:mTmG* mice showed dramatically reduced formation of aforementioned LPLCs, bile-duct like cells, and CK19$^+$ cells (Figures 1G–1I and Figure S2C). These results further confirmed an important role of Arid1a in facilitating LPLC formation from hepatocytes.

In addition to the AAV-Cre-mediated *Arid1a* deletion model, we further analyzed LPLC formation using *Albumin-Cre:Arid1a$^{f/f}$* (*Arid1a$^{\Delta li}$*) mice and *Mx-cre:Arid1a$^{f/f}$* (*Arid1a$^{\Delta li^*}$*) mice, in which *Arid1a* was deleted around birth and in adulthood by polyIC induction, respectively (Figures S2D and S2E). Both types of mice showed decreased numbers of LPLCs after DDC treatment as determined by Hnf4a and Sox9 staining (Figures S2F–S2I). Moreover, we analyzed whether Arid1a is involved in LPLC formation in other periportal liver injuries induced by 4,4-diaminodiphenylmethane (Limaye et al., 2010) and bile duct ligation (Yanger et al., 2013) (Figures S2J and S2L). In both injury models, the formation of Hnf4a$^+$Sox9$^+$ LPLCs was significantly attenuated in Arid1a-deficient mice (Figures S2K and S2M). We also analyzed CCl_4- and TAA-induced pericentral liver injuries; however, these injuries did not induce the LPLC formation (data not shown). These data supported the idea that a proper Arid1a function is required for LPLC formation in various periportal injuries.

Arid1a-Dependent Formation of Liver-Progenitor-Like Cells Contributes to Periportal-Injury-Induced Liver Regeneration

To determine the significance of Arid1a in liver regeneration, we first investigated the contribution of LPLCs to liver regeneration by labeling Hnf4a$^+$Sox9$^+$ cells in DDC-induced injury and tracing their fate during the recovery (Figure S3A). To label Hnf4a$^+$Sox9$^+$ cells, *Sox9-Cre^{ERT2}:Rosa26-frt-stop-frt-loxP-stop-loxP-RFP* (*Sox9- Cre^{ERT2}:Ai65D*) mice were used (Figure 2A, see STAR Methods). To delete the frt-stop-frt sequence from hepatocytes, we treated *Sox9-Cre^{ERT2}:Ai65D* mice with AAV2/8-TBG-Flp before DDC injury. Tamoxifen was then applied during the injury to remove the loxP-stop-loxP sequence and to label Hnf4a$^+$Sox9$^+$ cells as RFP$^+$ (Figure 2B). After tamoxifen treatment, 38.4% of DDC-induced Hnf4a$^+$Sox9$^+$ cells were specifically labeled as RFP$^+$ in the liver (Figure 2C). These mice were then kept on normal diet for 8 weeks of recovery. After the recovery, 9.3% of total hepatocytes were RFP$^+$ (Figure 2D). Correcting with the labeling efficiency, around 24.2% of hepatocytes (9.3%/38.4% = 24.2%) were derived from Hnf4a$^+$Sox9$^+$ cells in regenerated livers. In addition, we excluded the contribution of HybHP, a type of Sox9$^+$ hepatocyte detectable in *Sox9-Cre$^{ERT2:}$Rosa26-loxP-stop-loxP-RFP* (*Sox9-Cre^{ERT2}:RFP*) mice (Font-Burgada et al., 2015), to hepatocyte regeneration after DDC injury and recovery (Figures S3B and S3C, see STAR Methods). These data together suggest that injury-induced LPLCs contribute significantly to liver regeneration. Intriguingly, we identified a small percentage of RFP$^+$ bile duct cells (0.71%) in *Sox9-Cre^{ERT2}:Ai65D* mice after recovery (Figure S3D), supporting the idea that LPLCs gave rise to bile duct cells as well (Tanimizu et al., 2014; Tarlow et al., 2014b; Yanger et al., 2013).

Because the Arid1a deficiency blocks LPLC formation, we asked whether *Arid1a-KO* mice would display impaired liver regeneration (Figure 2E). We deleted *Arid1a* by AAV-Cre before DDC treatment (Figure 2F). We then subjected mice to a DDC diet for 2 weeks to induce LPLC formation and the mice then recovered on a normal diet for 8 weeks for regeneration. DDC-induced ductular reactions were resolved in both types of mice after the recovery as shown by CK19 staining (Figure S4A). In *Arid1a-WT* mice, livers were completely regenerated and most hepatocytes (99.7%) had already exited cell proliferation as determined by Ki67 (Figures 2G–2I). By contrast, DDC-induced hepatomegaly and hepatocyte hypertrophy (Figures S1F and S1G) were only partially resolved in *Arid1a-KO* mice

(C) Co-staining of RFP with Sox9 and Hnf4a in DDC-injured *Sox9-Cre^{ERT2}:Ai65D* reporter mice after DDC injury. Arrowheads indicated Hnf4a$^+$Sox9$^+$ cells that were labeled as RFP$^+$. The ratio of labeled Hnf4a$^+$Sox9$^+$RFP$^+$ cells to periportal Hnf4a$^+$Sox9$^+$ cells is shown (n = 2).

(D) Co-staining of RFP with Sox9 and Hnf4a in *Sox9-Cre^{ERT2}:Ai65D* reporter mice after the recovery. Note that Sox9 expression was diminished after recovery. The ratio of Hnf4a$^+$RFP$^+$ cells to total Hnf4a$^+$ cells is shown (n = 3).

(E–P) Experimental design of DDC-induced liver injury and recovery with *Arid1a* deletion before (E–J) or after (K–P) injury.

(E) *Arid1a* was deleted via tail vein injection of AAV-Cre (*Arid1a-KO*). *Arid1a$^{f/f}$* mice treated with AAV-GFP were used as a control (*Arid1a-WT*).

(F and L) Arid1a staining on liver sections from *Arid1a-WT* and *Arid1a-KO* mice at the time of sacrifice.

(G and M) Representative images of livers from *Arid1a-WT* and *Arid1a-KO* mice after recovery. Liver to body weight ratio was calculated.

(H and N) H&E staining on liver sections from *Arid1a-WT* and *Arid1a-KO* mice after recovery. Arrows indicate fatty changes in hepatocytes. The hepatocyte diameter was quantified and normalized to that of the *Arid1a-WT* control.

(I and O) Ki67 staining on liver sections. Arrowheads indicate Ki67$^+$ proliferating hepatocytes. The ratio of Ki67$^+$ hepatocytes to total hepatocytes per field of view is shown.

(J and P) Serum levels of ALT, AST, and ALP were measured after recovery.

n represents the number of animals for analyses. Data are presented as mean ± SEM; *$p < 0.05$, t test; scale bar represents 100 μm. See also Figures S3 and S4.

(Figures 2G and 2H), and a significant portion of hepatocytes continued to proliferate (Figure 2I). Moreover, *Arid1a-KO* livers showed remarkably increased accumulation of fatty vacuoles and impaired liver functions, both of which were absent in *Arid1a-WT* livers after recovery (Figures 2H and 2J). The defects in liver regeneration were also validated in $Arid1a^{\Delta li}$ mice (Figures S4B–S4H).

To analyze whether Arid1a has a role in recovery, we deleted the *Arid1a* allele specifically in the recovery (Figure 2K). In this experimental setting, Arid1a was not deleted during the injury, and DDC-induced LPLCs remained unchanged. AAV-Cre treatment after injury caused efficient and specific deletion of *Arid1a* in hepatocytes as shown by staining of Arid1a (Figure 2L) and lineage-specific markers (Figure S4I). After 8 weeks of recovery, mice with *Arid1a* deletion during the recovery showed liver sizes, hepatic architectures, liver functions, and hepatocyte proliferation comparable with those of with control mice (Figures 2M–2P). These results were reproduced using inducible $Arid1a^{\Delta li^*}$ mice in which *Arid1a* was deleted during the recovery (Figures S4J–S4N), thus largely excluding a role of Arid1a in recovery. Taken together, our findings support Arid1a-dependent LPLC formation contributing significantly to periportal-injury-induced liver regeneration.

Arid1a Controls Liver-Progenitor-Like Cell Formation through Chromatin Remodeling

Because Arid1a is important for chromatin opening, we characterized whether Arid1a regulates chromatin accessibility in LPLC-enriched genes by the assay for transposase-accessible chromatin using sequencing (ATAC-seq) (Buenrostro et al., 2015). DDC-injured hepatocytes were isolated by low-speed gravity centrifugation, and *Arid1a-KO* hepatocytes showed markedly less chromatin accessibility than *Arid1a-WT* hepatocytes throughout the whole genome (Figure S5A). We focused on analyzing the chromatin-accessible sites that were under the direct control of Arid1a by overlapping ATAC-seq peaks with published Arid1a ChIP-seq data in hepatocytes (Sun et al., 2016) (Figure S5B). In the 16,488 Arid1a-bound chromatin-accessible sites, we found that 53.1% sites (8,754, Group1 sites) showed reduced ATAC-seq peak signals after *Arid1a* deletion (Figure 3A and Figure S5C). Interestingly, when these sites were annotated with promoters and H3K4me1/H3K27ac-marked enhancers, Group1 sites were found to compose the greatest percentage of peaks located in enhancer regions (88.1%, Figure 3B), indicating that Group1 sites were enriched with transcriptional activation elements.

We next established a map between Arid1a-bound chromatin-accessible sites and their corresponding genes by the GREAT analysis (McLean et al., 2010) (see STAR Methods). Compared to genes mapped to Group2 and Group3 sites, GREAT analysis showed that LPLC conversion-related pathways were specifically enriched in genes mapped to Group1 sites (Table S4). Notably, 43% of Group1 sites (3,768 of 8,754) were mapped with 1,881 LPLC-enriched genes (hereafter called Arid1a-opened LPLC-enriched genes, Table S5), which accounted for 41.8% of the 4,505 LPLC-enriched genes (Figure 3C, $p = 7.93e{-}39$, Chi-square test). The chromatin-accessible sites in Arid1a-opened LPLC-enriched genes were located mainly at enhancer regions (89.5%, Figure S5D). Importantly, Arid1a-opened LPLC-enriched genes were composed of genes critical in LPLC formation, including the Hippo/Yap pathway (Figure 3D), which were dampened in *Arid1a-KO* mice (Table S5). The binding of Arid1a on LPLC-enriched genes was validated by ChIP-qPCR using the $Arid1a^{3xflag}$ mice at the resting condition and after DDC treatment for 3 days and 2 weeks (Figures S5E and S5F, Figure 3E, see STAR Methods). Moreover, in line with the attenuated chromatin accessibility at enhancer regions, Arid1a-opened LPLC-enriched genes showed remarkably reduced expression in DDC-injured *Arid1a-KO* livers (Figure 3F), some of which were confirmed by qPCR and immunostaining (Figure 3G and Figure S5G). These findings suggested that Arid1a controls chromatin accessibility of key LPLC-enriched genes.

We next analyzed whether the chromatin accessibility on Arid1a-opened LPLC-enriched genes was induced by liver injury. Strikingly, we found that 99.4% of chromatin-accessible sites (3,746 of 3,768) in Arid1a-opened LPLC-enriched genes showed high ATAC-seq peak signals before DDC treatment in *Arid1a-WT* hepatocytes (Figure 4A), as exemplified by critical genes in LPLC conversion-related pathways (Figures 4B–4E). These data indicated that Arid1a-opened LPLC-enriched genes were already accessible in the resting condition, implying a permissive chromatin status prior to injury. We also analyzed chromatin accessibility in $Sox9^+$ LPLCs, which were isolated from DDC-injured *Sox9-*Cre^{ERT2}*:RFP* mice (see STAR Methods). The progenitor status of $Sox9^+$ hepatocytes was confirmed by the expression of LPLC-enriched genes and a partial shift of the chromatin status from hepatocytes to bile duct cells (Figures S5H and S5I, see STAR Methods). As expected, the chromatin status at Arid1a-opened LPLC-enriched genes was comparably opened among normal hepatocytes, DDC-injured hepatocytes, and $Sox9^+$ LPLCs (Figures 4A–4E). Importantly, *Arid1a* deletion caused reduced ATAC-seq signals in these peaks independent of DDC treatment (Figures 4A–4E), suggesting that Arid1a is required to actively maintain the permissive chromatin status at these LPLC-enriched genes under the resting condition.

Arid1a-Dependent Permissive Chromatin Renders Hepatocyte Competence in Responding to the Hippo/Yap Signal

Given that chromatin accessibility facilitates gene transcription (Wilson and Roberts, 2011), we postulated that the permissive chromatin status at Arid1a-opened LPLC-enriched genes might endow hepatocytes competent to respond quickly to injury-signal-induced transcription. Accordingly, the formation of LPLCs *in vivo*, initiated as early as 3 days after injury (Figure S1L and Figure S3A), is faster than transcription-factor-induced cell identity conversion *in vitro*, which often takes 1–3 weeks (Takahashi and Yamanaka, 2006; Xu et al., 2015). Among the several LPLC conversion-related pathways, the Hippo/Yap pathway was one of the most enriched (Figure 3D). MOTIF analysis predicted that chromatin-accessible sites of Arid1a-opened LPLC-enriched genes composed DNA sequences bound by TEAD (Figure S5J), the downstream transcription factor of the Hippo/Yap pathway (Piccolo et al., 2014). Liver-enriched transcription factors, such as Foxa2 and Hnf1b, and AP-1 genes were found to be enriched as well (Figure S5J). Importantly, GSEA analysis showed that Hippo/Yap-related progenitor signature genes (Cordenonsi et al., 2011) were suppressed in *Arid1a-KO* livers (Figure S5K), which was validated by qPCR

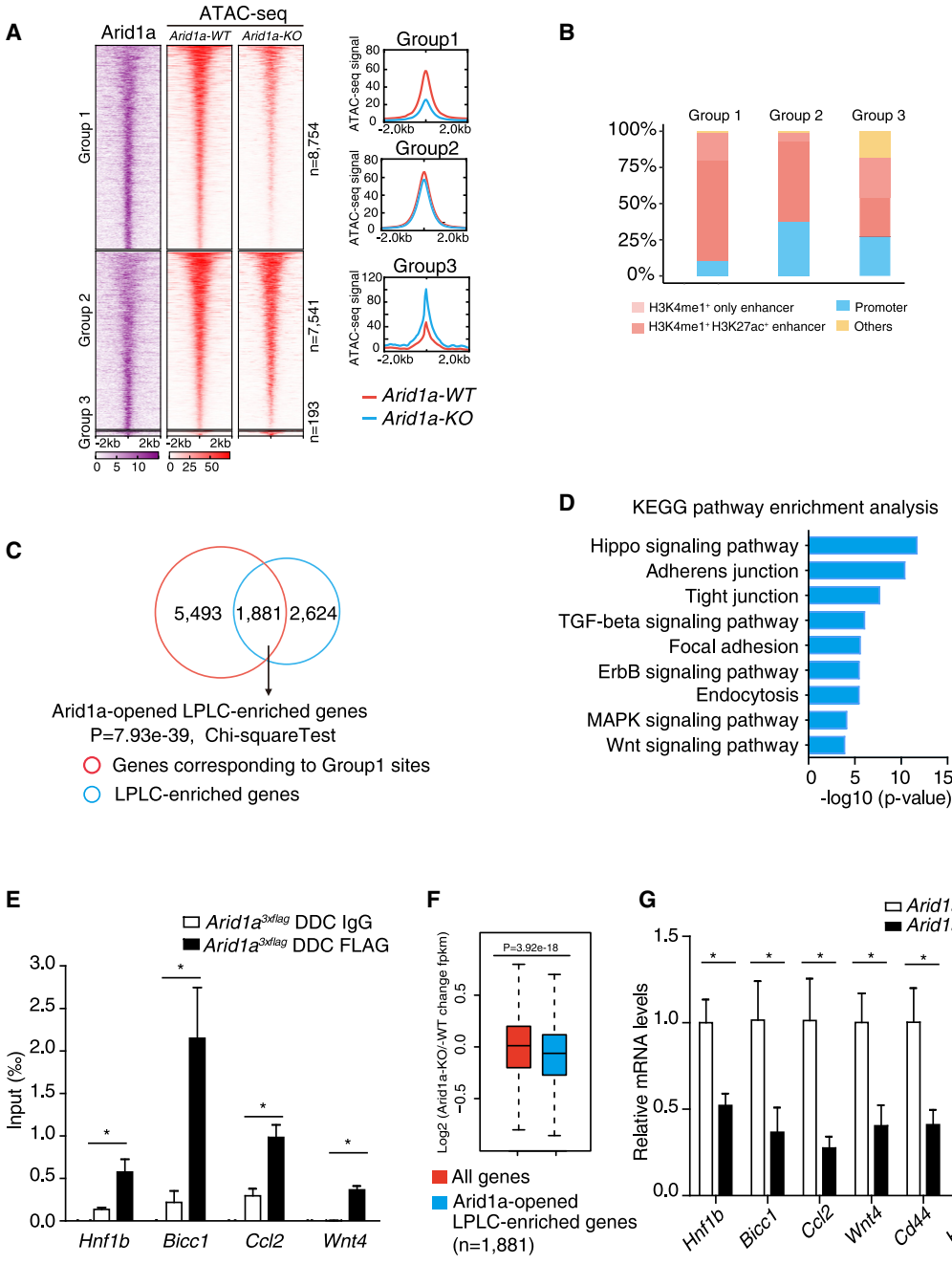

Figure 3. Arid1a Controls Liver-Progenitor-Like Cell Formation through Chromatin Remodeling

(A) Hepatocytes were isolated after 2 weeks of DDC treatment, and ATAC-seq was performed. Heatmaps of Arid1a ChIP-seq (Sun et al., 2016) and ATAC-seq peak signals on 16,488 Arid1a-bound chromatin-accessible sites are shown. ATAC-seq peaks were clustered into three groups based on the change of ATAC peak signals between DDC-injured *Arid1a-WT* and *Arid1a-KO* hepatocytes (1.5-fold change). Average ATAC-seq peak signals are presented for the three groups on the right panels.

(B) Distribution of genomic features of Arid1a-bound chromatin-accessible sites in the three groups in (A) as annotated with promoters, H3K4me1/H3K27ac enhancers, and others.

(C) Overlap of genes corresponding to Group1 sites with LPLC-enriched genes. These genes were defined as Arid1a-opened LPLC-enriched genes.

(D) The KEGG pathway enrichment analysis of Arid1a-opened LPLC-enriched genes. LPLC conversion-related pathways were highly enriched.

(E) ChIP-qPCR validation of the binding of Arid1a on Arid1a-opened LPLC-enriched genes in *Arid1a*^{3xflag} hepatocytes (n = 3 for each group) after DDC injury for 2 weeks.

(F) Expression levels of Arid1a-opened LPLC-enriched genes in *Arid1a-WT* and *Arid1a-KO* livers after 2 weeks of DDC treatment. Wilcoxon rank sum test was applied.

(G) qPCR analyses of Arid1a-opened LPLC-enriched genes in 2 weeks of DDC-injured *Arid1a-WT* and *Arid1a-KO* hepatocytes.

Data were presented as mean ± SEM; *p < 0.05, t test. See also Figure S5.

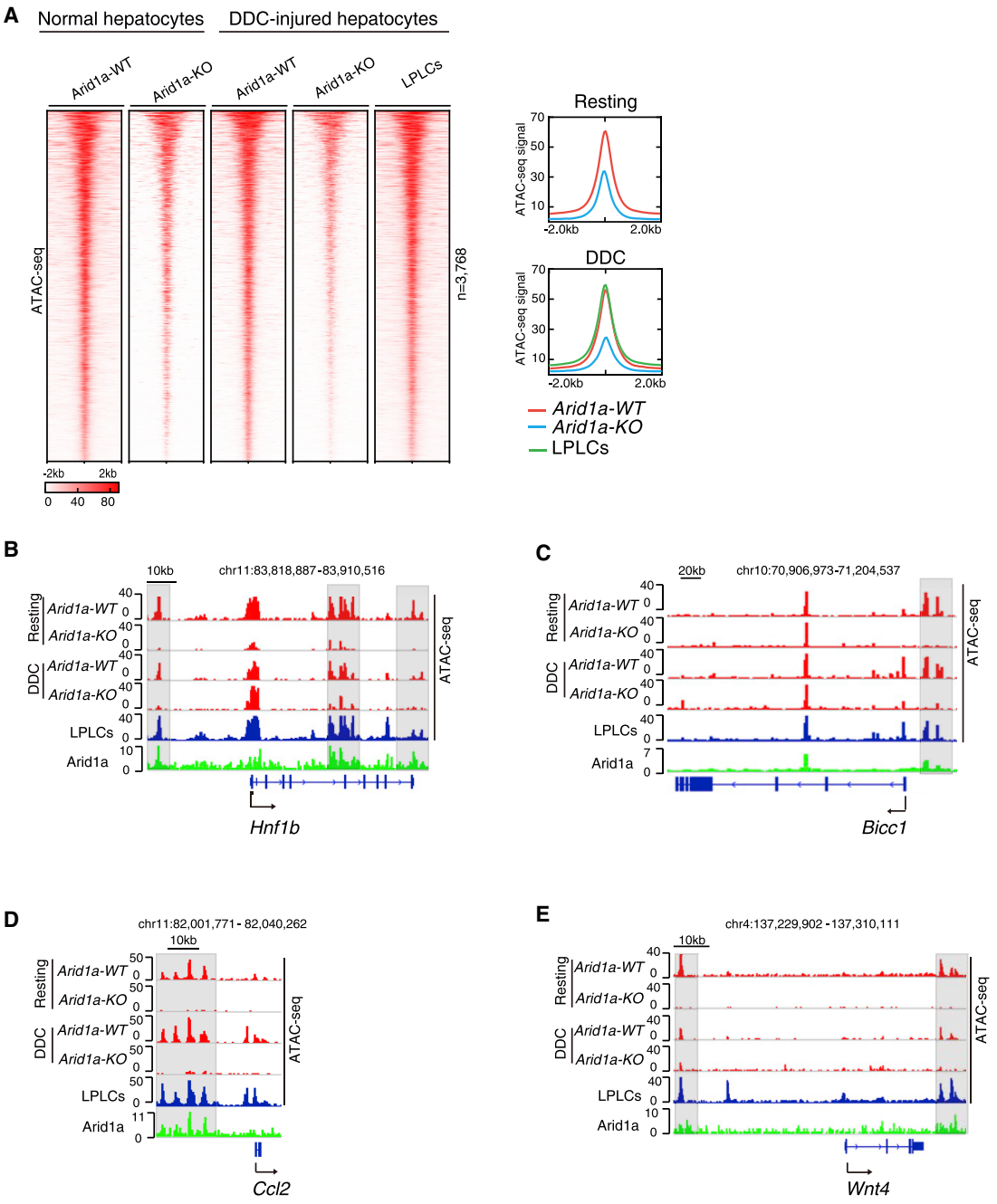

Figure 4. Arid1a-Dependent Permissive Chromatin Status Underlies a Competence in Liver-Progenitor-Like Cell Formation

(A) Heatmaps of ATAC-seq peak signals of 3,768 chromatin-accessible sites in Arid1a-opened LPLC-enriched genes. ATAC-seq peak signals were shown in *Arid1a-WT* and *Arid1a-KO* hepatocytes under the resting condition, DDC-injured *Arid1a-WT* and *Arid1a-KO* hepatocytes, and *Arid1a* wild-type Sox9$^+$ LPLCs after 2 weeks of DDC treatment. Average ATAC-seq peak signals are presented on the right panel.

(B–E) ATAC-seq and Arid1a ChIP-seq signal tracks near the LPLC-enriched gene loci are shown in *Arid1a-WT* and *Arid1a-KO* hepatocytes under the resting condition, DDC-injured *Arid1a-WT* and *Arid1a-KO* hepatocytes, and *Arid1a* wild-type Sox9$^+$ LPLCs after 2 weeks of DDC treatment. The ATAC-seq signals of representative LPLC-enriched genes, involving biliary function (B), the Hippo pathway (C), the inflammatory pathway (D), and the Wnt pathway (E), are shown. Shaded regions are representative permissive chromatin sites.

See also Figure S5.

(Figure S5L). These data suggested that Arid1a-opened permissive chromatin likely renders hepatocytes competent to respond to Hippo/Yap signaling.

Yap is the critical regulatory factor of the Hippo/Yap pathway. Upon activation, Yap first translocates into the nucleus and then binds to its target genes to trigger their transcription

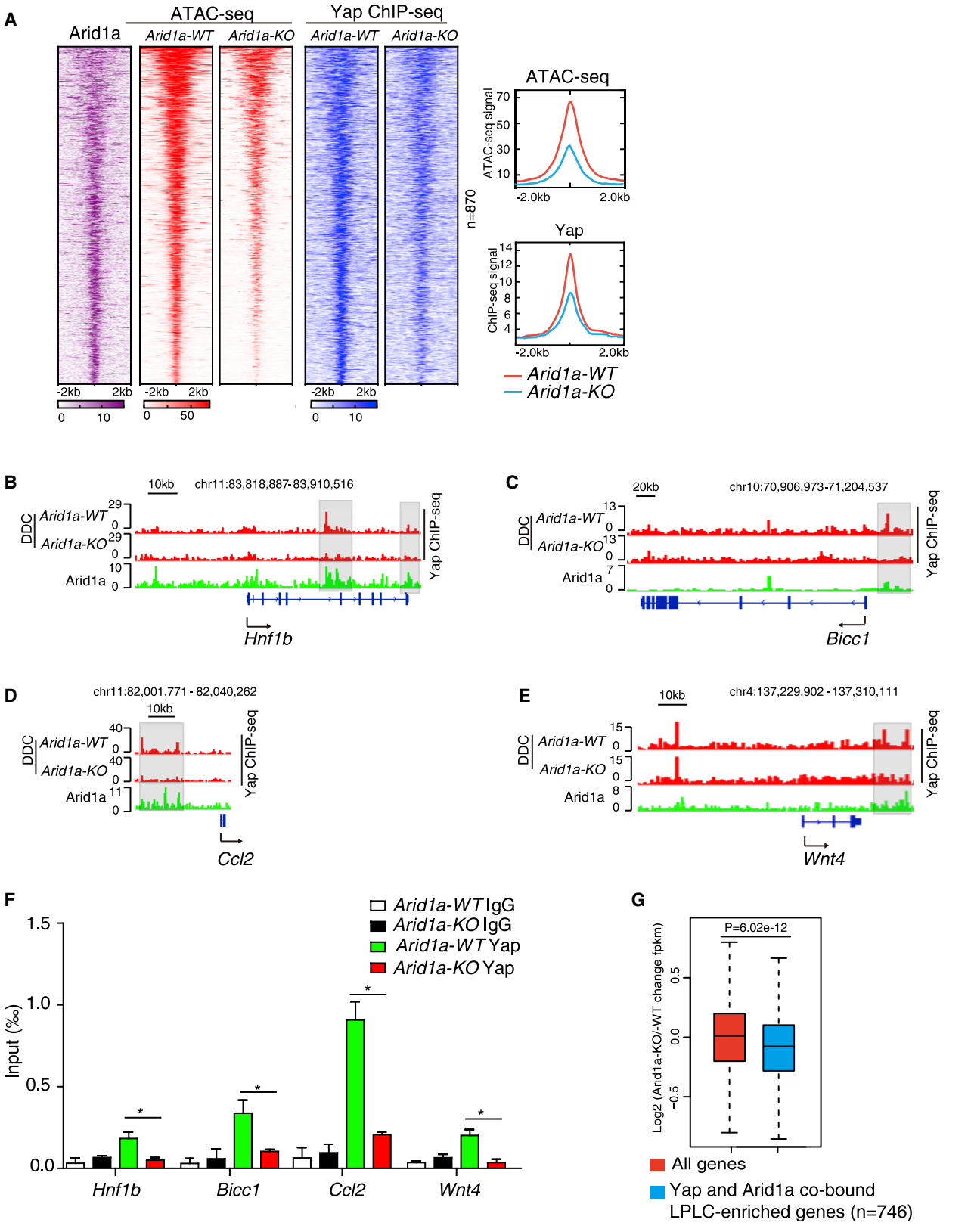

(legend on next page)

(Piccolo et al., 2014). In both *Arid1a-WT* and *Arid1a-KO* hepatocytes, we found that Yap was stabilized and translocated into the nucleus after DDC injury (Figures S6A and S6B). Nuclear translocation of Yap was further validated in both types of mice by immunostaining (Figures S6C and S6D, see STAR Methods). These data suggested that Arid1a is not required in the upstream activation of the Hippo/Yap pathway. We then asked whether Arid1a-opened permissive chromatin might facilitate Yap binding to LPLC-enriched genes. To that end, we performed Yap ChIP-seq and compared its binding in DDC-injured *Arid1a-WT* and *Arid1a-KO* hepatocytes. In line with DDC-induced LPLC formation, a proportion of Yap (17.2%) was found to bind to chromatin sites specifically accessible in bile duct cells. Importantly, the genomic distribution of Arid1a and Yap revealed that a significant fraction of Yap binding sites were co-localized with Arid1a on chromatin-accessible sites (Figure S6E). The co-localization of Arid1a and Yap was further supported by the protein immunoprecipitation assay (Figure S6F). For those chromatin sites that showed reduced accessibility in DDC-injured *Arid1a-KO* mice, the binding of Yap was accordingly decreased (Figure S6G). When Arid1a-opened LPLC-enriched genes were specifically analyzed, 23.1% of Arid1a-bound chromatin-accessible sites were found to be co-bound by Yap (870 of 3,768, $p = 1.2e-181$, Chi-square test, Figure 5A). These co-bound sites mapped to 746 genes accounted for 39.7% of 1,881 Arid1a-opened LPLC-enriched genes. Along with decreased chromatin accessibility of these co-bound sites in DDC-injured *Arid1a-KO* hepatocytes, we found that the Yap binding was remarkably reduced (Figure 5A), as exemplified by critical genes in LPLC conversion-related pathways (Figures 5B–5E and referred to in Figures 4B–4E). The reduced binding of Yap to these sites was validated by ChIP-qPCR (Figure 5F). Moreover, expression levels of these co-bound genes were decreased in *Arid1a-KO* mice (Figure 5G). These data suggested that Arid1a prepares a permissive chromatin status to facilitate Yap-mediated transcription from LPLC-enriched genes, thus providing a molecular basis for hepatocyte competence in responding to regenerative signals.

Arid1a-Dependent Yap Transcriptional Activation Regulates Liver-Progenitor-Like Cell Formation *In Vivo*

Finally, we analyzed whether Arid1a endowed competence to respond to the Hippo/Yap signal functionally important for LPLC formation. We first determined the requirement of Yap in the induction of LPLCs using AAV-Cre-treated $Yap^{f/f}$ mice (*Yap-KO*) (Figure 6A). *Yap-KO* mice showed impaired serum biochemical indexes after DDC injury and recovery (Figures S6H and S6I), suggesting defects in liver injury and regeneration. Importantly, the number of DDC-induced LPLCs was significantly lower in *Yap-KO* livers than in *Yap-WT* mice (Figure 6B). Expression analyses of Sox9 and LPLC-enriched genes confirmed the reduced LPLC formation in *Yap-KO* livers after DDC injury (Figure 6C). These results indicated the key role of Yap in triggering LPLC formation under liver injury.

We next established a Yap-induced LPLC model by overexpressing the constitutive active YapS127A in hepatocytes via a sleeping beauty transposon system (Chen and Calvisi, 2014; Yimlamai et al., 2014) (Figure 6D). YapS127A was specifically overexpressed in hepatocytes by hydrodynamic delivery as shown in AAV-Cre-treated *mTmG* mice (Figure S6J), and Arid1a deficiency showed no effect on the genomic integration of YapS127A (Figure S6K). The formation of $Hnf4a^{+}Sox9^{+}$ cells was detectable at 8 weeks and 12 weeks of YapS127A overexpression (Figure 6E). Compared with $Arid1a^{f/f}$ control mice, *Arid1a* deletion significantly decreased the formation of $Yap^{+}Sox9^{+}$ cells (Figure 6F). Taken together, these data indicate that Arid1a endows hepatocytes with critical competence in responding to Yap-induced LPLC formation *in vivo*.

DISCUSSION

Hepatocyte-Derived Progenitor-Like Cells and Liver Regeneration

In periportal injured livers, hepatocytes could convert into LPLCs and re-differentiate into functional hepatocytes after damage subsides (Tanimizu et al., 2014; Tarlow et al., 2014b; Yanger et al., 2013). Hepatocyte to LPLC conversion has received great attention since discovered and has been considered as an important cellular source for liver regeneration. We showed a significant role of Arid1a-dependent hepatocyte to LPLC conversion in periportal injuries. Arid1a deficiency in hepatocytes leads to impaired formation of LPLCs and abnormal regeneration in injured liver tissues, supporting the contribution of hepatocyte plasticity in liver repair. This might be clinically relevant, because it has been demonstrated that human liver diseases are often associated with the formation of LPLCs (Sirica, 1995; Yanger et al., 2013).

Previous study showed that Arid1a deficiency promotes liver regeneration after surgical resection and chemical-induced pericentral injuries via reducing pericentral chemical metabolism and increasing hepatocyte proliferation (Sun et al., 2016). Regarding DDC-induced periportal injury, previous study (Sun et al., 2016) and our results both showed that Arid1a deficiency led to increased hepatomegaly and other consistent phenotypes under DDC injury. We additionally showed that Arid1a deficiency blocked the formation of LPLCs. Notably, hepatocyte

Figure 5. Permissive Chromatin Renders Hepatocytes Competent to Respond to the Hippo/Yap Signal

(A) Heatmaps of Arid1a ChIP-seq, ATAC-seq, and Yap ChIP-seq signals of 870 Arid1a and Yap co-bound chromatin-accessible sites in Arid1a-opened LPLC-enriched genes. ATAC-seq and Yap ChIP-seq were performed in *Arid1a-WT* and *Arid1a-KO* hepatocytes after 2 weeks of DDC treatment. Average ATAC-seq and Yap ChIP-seq signals are shown on the right panels.

(B–E) Yap and Arid1a ChIP-seq signal tracks near LPLC-enriched gene loci are shown in *Arid1a-WT* and *Arid1a-KO* hepatocytes after 2 weeks of DCC treatment. Shaded regions are Yap and Arid1a co-bound sites.

(F) ChIP-qPCR validation of the binding of Yap on LPLC-enriched genes in DDC-injured hepatocytes (n = 3 for each group).

(G) The expression levels of Yap and Arid1a co-bound LPLC-enriched genes are compared between *Arid1a-WT* and *Arid1a-KO* livers after 2 weeks of DDC treatment. Wilcoxon rank sum test was applied.

Data are presented as mean ± SEM; *$p < 0.05$, t test. See also Figure S6.

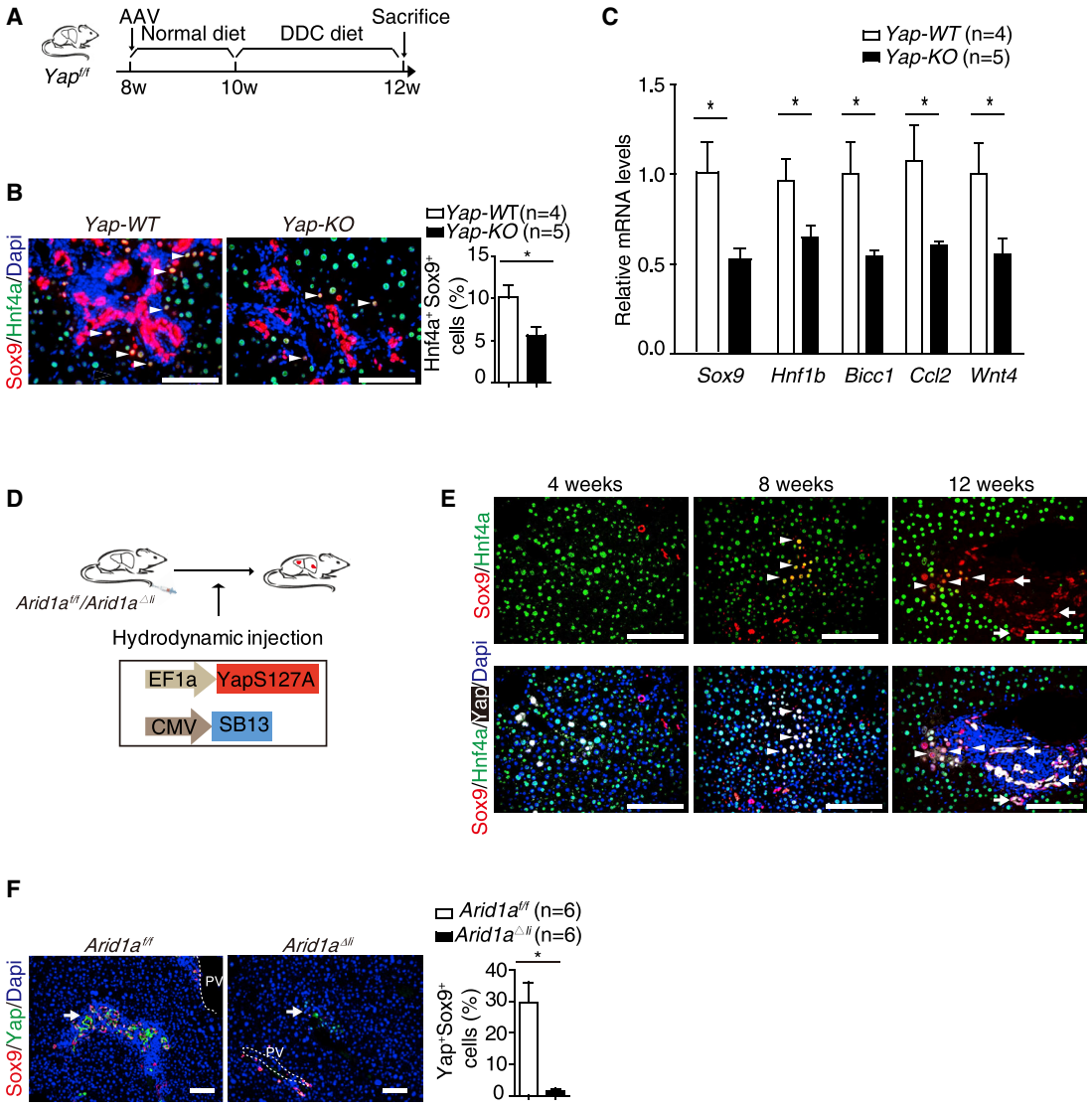

Figure 6. Arid1a Facilitates Yap in Forming Liver-Progenitor-Like Cells *In Vivo*

(A) Experimental design of DDC-induced hepatocyte to LPLC conversion. *Yap* was deleted via tail vein injection of AAV-Cre (*Yap-KO*), and *Yap*$^{f/f}$ mice treated with AAV-GFP were used as a control (*Yap-WT*).

(B) Co-staining of Hnf4a and Sox9 in *Yap-WT* and *Yap-KO* mouse livers after 2 weeks of DDC treatment. Arrowheads indicate Hnf4a$^+$Sox9$^+$ LPLCs. The ratio of Hnf4a$^+$Sox9$^+$ hepatocytes to Hnf4a$^+$ hepatocytes per periportal field of view is shown.

(C) qPCR detection of LPLC-enriched genes in *Yap-WT* and *Yap-KO* livers after 2 weeks of DDC treatment.

(D) Experimental design of constitutive active YapS127A-induced hepatocyte to LPLC conversion.

(E) Co-staining of Sox9, Hnf4a, and Yap in *Arid1a*$^{f/f}$ livers after hydrodynamic injection of YapS127A. Arrowheads indicate Yap$^+$Hnf4a$^+$Sox9$^+$ cells. Interestingly, Yap$^+$Hnf4a$^-$Sox9$^+$ cells (indicated by arrows) were detectable 12 weeks after YapS127A overexpression.

(F) Co-staining of Yap and Sox9 in *Arid1a*$^{f/f}$ and *Arid1a*$^{\Delta/\Delta}$ mice 12 weeks after YapS127A overexpression. Arrows indicate clones of Yap$^+$Sox9$^+$ LPLCs, which were largely missing in *Arid1a*$^{\Delta/\Delta}$ livers. The ratio of Yap$^+$Sox9$^+$ cells to Yap$^+$ cells is shown.

n represents the number of animals for analyses. Data are presented as mean ± SEM; *p < 0.05, t test; scale bar represents 100 μm. See also Figure S6.

proliferation and cell death were comparable between *Arid1a-WT* and *Arid1a-KO* livers under DDC injury, and Arid1a deficiency blocked the direct overexpression of Yap-induced LPLCs, suggesting that reduced LPLC formation in *Arid1a-KO* livers appeared to be a consequence of Arid1a deficiency. We also uncovered that Arid1a deficiency triggered hepatocyte hypertrophy, which is a compensative mechanism of liver regeneration (Miyaoka et al., 2012) and likely provides a plausible explanation for hepatomegaly and other phenotypes in *Arid1a-KO* mice under DDC injury. Previous study (Sun et al., 2016) specifically deleted Arid1a before the recovery and found enhanced hepatocyte proliferation in *Arid1a-KO* mice after 10 days recovery. Following the same protocol, we extended the recovery to 8 weeks and found that both *Arid1a-KO* and *Arid1a-WT* mice show comparable proliferation and liver regeneration, suggesting a transient role of Arid1a in proliferation during

recovery. The targets of Arid1a appeared to be different as well. Whereas Sun et al. suggested a CYP-metabolism-dependent mechanism in pericentral injuries, we found that Arid1a regulated LPLC-enriched genes, some of which, including Ccl2 and Csf1, were reported to be involved in hepatocyte plasticity (Guo et al., 2017). Therefore, our study and others reveal multiple functions of Arid1a in liver regeneration, i.e., a facilitator of LPLC formation during injury and a transient obstructer of proliferation in recovery. Nevertheless, further characterization of the Arid1a-regulated downstream targets might shed light on the development of cell-identity-conversion-based therapies for liver diseases related to impaired hepatocyte regeneration.

In Vivo and *In Vitro* Cell Identity Conversion

Induction of pluripotency and other functional cells demonstrates that cell identity conversion can be achieved by lineage-specific transcription factors (Takahashi and Yamanaka, 2006; Xu et al., 2015). Previous studies showed that the chromatin accessibility of cell-identity-conversion-related genes is remarkably remodeled during *in vitro* reprogramming (Li et al., 2017; Stadhouders et al., 2018). We found previously that the extensive chromatin opening induced by transcription factors activated the ATM/p53 pathway in transdifferentiation from fibroblasts to hepatocytes (Ji et al., 2017). The cellular response to eliminating cells undergoing remarkable chromatin opening in cell identity conversion is termed the "chromatin remodeling checkpoint," which serves as a mechanism to restrict cell identity change (Zaret, 2017). By contrast, we here demonstrated that the chromatin accessibility of LPLC-enriched genes is already at permissive status in hepatocytes under the resting condition, indicating a primed chromatin status during *in vivo* cell identity conversion. This permissive chromatin might provide an epigenetic explanation as to why remarkable transcription of lineage genes can lead to reprogramming of differentiated cells in injured tissues rather than activation of the chromatin remodeling checkpoint to restrict cell identity conversion *in vivo*.

Intriguingly, YapS127A-induced cell identity conversion took longer than DDC injury-induced LPLC formation. It is possible that besides the Hippo/Yap pathway, DDC injury triggered the activation of multiple pathways involved in this process (Tarlow et al., 2014b). Moreover, compared to YapS127A overexpression, DDC injury caused extensive stromal cell activation and tissue structure remodeling, which may provide microenvironment cues facilitating cell identity conversion.

Permissive Chromatin Renders a Competence in Responding to Regenerative Signals

Reprogramming of differentiated cells for regeneration is well demonstrated in other epithelia organs in addition to the liver, such as the intestine and the pancreas (Kopp et al., 2016; Tetteh et al., 2016). In the intestine, depletion of Lgr5$^+$ stem cells causes secretory and absorptive progenitors to dedifferentiate to Lgr5$^+$ cells (Tetteh et al., 2016). In the pancreas, extreme β cell loss causes α-cell-to-β-cell conversion for pancreas regeneration (Kopp et al., 2016). The cell plasticity in multiple epithelia tissues raises an open question about the underlying mechanism of reprogramming. While certain developmental and regenerative pathways were identified in regulating reprogramming, there might exist some general principles underlying cell plasticity (Clevers and Watt, 2018).

We here demonstrated an important role of Arid1a-dependent permissive chromatin at LPLC-enriched genes in establishing hepatocyte competence to respond to regenerative signals. The permissive chromatin status is maintained prior to the injury-induced LPLC formation. Loss of permissive chromatin status restricts hepatocyte to LPLC conversion. Interestingly, retrospective analyses of previous studies on chromatin status in intestinal and pancreatic cells indicate the possible existence of permissive chromatin in these epithelia cells. In intestinal crypts, chromatin accessible sites are largely overlapped among intestinal secretory progenitors, absorptive progenitors, and Lgr5$^+$ stem cells, and the chromatin of key stem cell-related genes, including *Lgr5*, *Bmi1*, *Lrig1*, and *Ascl2*, is retained as permissive in secretory and absorptive progenitors under the resting condition (Jadhav et al., 2017; Kim et al., 2014). Similarly, 95.6% of the chromatin accessible sites in pancreatic β cells, including key regulatory genes Pdx1 and MafA, are accessible in α cells under the resting condition (Ackermann et al., 2016). In acinar cells, the chromatin of key transcription factor Sox9, which regulates acinar cells to duct cell reprogramming, is also retained as permissive (Ackermann et al., 2016). Interestingly, a recent study also showed that about half of chromatin accessible sites in the surfactant-producing alveolar type 2 cells were shared with the Axin2$^+$ alveolar epithelial progenitors in the distal lung (Zacharias et al., 2018). Our data and that of others together indicate that differentiated cells can retain the permissive chromatin of cells from developmentally close lineages, which may serve as an intrinsic epigenetic mechanism for competence in cell identity conversion.

Permissive chromatin is a part of the transcriptional activation mechanism that responds to environmental cues in embryonic development (Gualdi et al., 1996; Lindeman et al., 2011; Wang et al., 2015; Xu et al., 2011), also known as developmental competence. It is remarkable that both embryonic development and hepatocyte to LPLC conversion employ a common molecular paradigm to interpret extrinsic signals. As the plasticity of stem cells declines and chromatin accessibility reduces in aged cells (Sen et al., 2016), it would be interesting to establish whether permissive-chromatin-dependent reprogramming is retained in aged tissues. It thus would provide a plausible epigenetic basis to harness cell plasticity to enhance regeneration of aged tissues. It is also worth analyzing whether the permissive chromatin is evolutionarily variable; it may serve as a molecular explanation for the different regeneration capabilities among vertebrates.

STAR★METHODS

Detailed methods are provided in the online version of this paper and include the following:

- KEY RESOURCES TABLE
- LEAD CONTACT AND MATERIALS AVAILABILITY
- EXPERIMENTAL MODEL AND SUBJECT DETAILS
  - Mice
  - Lineage tracing of liver progenitor-like cells and HybHP in DDC-induced periportal liver regeneration

SUPPLEMENTAL INFORMATION

Supplemental Information can be found online at https://doi.org/10.1016/j.stem.2019.06.008.

ACKNOWLEDGMENTS

We are thankful to Kenneth S. Zaret (University of Pennsylvania) and Naihe Jing (SIBCB, CAS, China) for developing the concept of reprogramming competence; Hao Zhu (UT Southwestern Medical Center) for the Arid1a ChIP-seq data, protocol, and discussion; and Yi A. Zeng (SIBCB, CAS, China), Naihe Jing, Gang Wei (PICB, CAS, China), and Fei Lan (Fudan University, China) for critical comments. We thank Duojia Pan (HHMI, UT Southwestern Medical Center) for *Yap*$^{f/f}$ mice and Xin Chen (UCSF) for sleeping beauty transposon plasmids. We also thank the core facilities for molecular biology, cell biology, and animal care at SIBCB. This study is supported by Chinese Academy of Sciences (XDA16020201 and XDA12050104), the National Natural Science Foundation of China (31630044, 31601186, 81703093, and 31801228), Science and Technology Commission of Shanghai Municipality (16JC1400202), National Major Science and Technology Projects of China (2018ZX09711002-009), and National Special Support Plan for Top Talents.

AUTHOR CONTRIBUTIONS

W.L. and L.H. designed the study. W.L. and C.H. initiated the project, and W.L. performed most of the experiments. X.D., X.Z., W.F.Xie, and Z.W. generated mouse models. L.Y., H.L., and Y.L. performed bioinformatics analysis. W.L., Y.C., L. Zhu, and Xiolong Ma performed the ATAC-seq and ChIP-seq assays. W.L., J.C., Q.H., and C.H. performed mouse experiments. S.B., Xueyan Ma, and L. Zhang performed the immunoblot assays. W.L. and L.H. analyzed the data and wrote the manuscript.

DECLARATION OF INTERESTS

The authors declare no competing interests.

Received: August 23, 2018
Revised: February 23, 2019
Accepted: June 13, 2019
Published: July 3, 2019

REFERENCES

Ackermann, A.M., Wang, Z., Schug, J., Naji, A., and Kaestner, K.H. (2016). Integration of ATAC-seq and RNA-seq identifies human alpha cell and beta cell signature genes. Mol. Metab. *5*, 233–244.

Apostolou, E., and Hochedlinger, K. (2013). Chromatin dynamics during cellular reprogramming. Nature *502*, 462–471.

Blanpain, C., and Fuchs, E. (2014). Stem cell plasticity. Plasticity of epithelial stem cells in tissue regeneration. Science *344*, 1242281.

Buenrostro, J.D., Wu, B., Chang, H.Y., and Greenleaf, W.J. (2015). ATAC-seq: A Method for Assaying Chromatin Accessibility Genome-Wide. Curr. Protoc. Mol. Biol. *109*, 21–29.

Chen, X., and Calvisi, D.F. (2014). Hydrodynamic transfection for generation of novel mouse models for liver cancer research. Am. J. Pathol. *184*, 912–923.

Chen, J., Liu, H., Liu, J., Qi, J., Wei, B., Yang, J., Liang, H., Chen, Y., Chen, J., Wu, Y., et al. (2013). H3K9 methylation is a barrier during somatic cell reprogramming into iPSCs. Nat. Genet. *45*, 34–42.

Clevers, H., and Watt, F.M. (2018). Defining Adult Stem Cells by Function, not by Phenotype. Annu. Rev. Biochem. *87*, 1015–1027.

Corces, M.R., Trevino, A.E., Hamilton, E.G., Greenside, P.G., Sinnott-Armstrong, N.A., Vesuna, S., Satpathy, A.T., Rubin, A.J., Montine, K.S., Wu, B., et al. (2017). An improved ATAC-seq protocol reduces background and enables interrogation of frozen tissues. Nat. Methods *14*, 959–962.

Cordenonsi, M., Zanconato, F., Azzolin, L., Forcato, M., Rosato, A., Frasson, C., Inui, M., Montagner, M., Parenti, A.R., Poletti, A., et al. (2011). The Hippo transducer TAZ confers cancer stem cell-related traits on breast cancer cells. Cell *147*, 759–772.

Dorrell, C., Erker, L., Lanxon-Cookson, K.M., Abraham, S.L., Victoroff, T., Ro, S., Canaday, P.S., Streeter, P.R., and Grompe, M. (2008). Surface markers for the murine oval cell response. Hepatology *48*, 1282–1291.

Eroglu, E., Burkard, T.R., Jiang, Y., Saini, N., Homem, C.C.F., Reichert, H., and Knoblich, J.A. (2014). SWI/SNF complex prevents lineage reversion and induces temporal patterning in neural stem cells. Cell *156*, 1259–1273.

Font-Burgada, J., Shalapour, S., Ramaswamy, S., Hsueh, B., Rossell, D., Umemura, A., Taniguchi, K., Nakagawa, H., Valasek, M.A., Ye, L., et al. (2015). Hybrid Periportal Hepatocytes Regenerate the Injured Liver without Giving Rise to Cancer. Cell *162*, 766–779.

Gao, X., Tate, P., Hu, P., Tjian, R., Skarnes, W.C., and Wang, Z. (2008). ES cell pluripotency and germ-layer formation require the SWI/SNF chromatin remodeling component BAF250a. Proc. Natl. Acad. Sci. USA *105*, 6656–6661.

Gualdi, R., Bossard, P., Zheng, M., Hamada, Y., Coleman, J.R., and Zaret, K.S. (1996). Hepatic specification of the gut endoderm in vitro: cell signaling and transcriptional control. Genes Dev. *10*, 1670–1682.

Guichard, C., Amaddeo, G., Imbeaud, S., Ladeiro, Y., Pelletier, L., Maad, I.B., Calderaro, J., Bioulac-Sage, P., Letexier, M., Degos, F., et al. (2012). Integrated analysis of somatic mutations and focal copy-number changes identifies key genes and pathways in hepatocellular carcinoma. Nat. Genet. *44*, 694–698.

Guo, X., Zhao, Y., Yan, H., Yang, Y., Shen, S., Dai, X., Ji, X., Ji, F., Gong, X.G., Li, L., et al. (2017). Single tumor-initiating cells evade immune clearance by recruiting type II macrophages. Genes Dev. *31*, 247–259.

Heinz, S., Benner, C., Spann, N., Bertolino, E., Lin, Y.C., Laslo, P., Cheng, J.X., Murre, C., Singh, H., and Glass, C.K. (2010). Simple combinations of lineage-determining transcription factors prime cis-regulatory elements required for macrophage and B cell identities. Mol. Cell *38*, 576–589.

Jadhav, U., Saxena, M., O'Neill, N.K., Saadatpour, A., Yuan, G.C., Herbert, Z., Murata, K., and Shivdasani, R.A. (2017). Dynamic Reorganization of Chromatin Accessibility Signatures during Dedifferentiation of Secretory Precursors into Lgr5+ Intestinal Stem Cells. Cell Stem Cell *21*, 65–77 e65.

Jain, R., Barkauskas, C.E., Takeda, N., Bowie, E.J., Aghajanian, H., Wang, Q., Padmanabhan, A., Manderfield, L.J., Gupta, M., Li, D., et al. (2015). Plasticity of Hopx(+) type I alveolar cells to regenerate type II cells in the lung. Nat. Commun. *6*, 6727.

Ji, S., Zhu, L., Gao, Y., Zhang, X., Yan, Y., Cen, J., Li, R., Zeng, R., Liao, L., Hou, C., et al. (2017). Baf60b-mediated ATM-p53 activation blocks cell identity conversion by sensing chromatin opening. Cell Res. *27*, 642–656.

Kim, T.H., Li, F., Ferreiro-Neira, I., Ho, L.L., Luyten, A., Nalapareddy, K., Long, H., Verzi, M., and Shivdasani, R.A. (2014). Broadly permissive

intestinal chromatin underlies lateral inhibition and cell plasticity. Nature *506*, 511–515.

Koche, R.P., Smith, Z.D., Adli, M., Gu, H., Ku, M., Gnirke, A., Bernstein, B.E., and Meissner, A. (2011). Reprogramming factor expression initiates widespread targeted chromatin remodeling. Cell Stem Cell *8*, 96–105.

Kopp, J.L., Grompe, M., and Sander, M. (2016). Stem cells versus plasticity in liver and pancreas regeneration. Nat. Cell Biol. *18*, 238–245.

Kühn, R., Schwenk, F., Aguet, M., and Rajewsky, K. (1995). Inducible gene targeting in mice. Science *269*, 1427–1429.

Langmead, B., and Salzberg, S.L. (2012). Fast gapped-read alignment with Bowtie 2. Nat. Methods *9*, 357–359.

Lessard, J.A., and Crabtree, G.R. (2010). Chromatin regulatory mechanisms in pluripotency. Annu. Rev. Cell Dev. Biol. *26*, 503–532.

Li, D., Fu, J., Du, M., Zhang, H., Li, L., Cen, J., Li, W., Chen, X., Lin, Y., Conway, E.M., et al. (2016). Hepatocellular carcinoma repression by TNFα-mediated synergistic lethal effect of mitosis defect-induced senescence and cell death sensitization. Hepatology *64*, 1105–1120.

Li, D., Liu, J., Yang, X., Zhou, C., Guo, J., Wu, C., Qin, Y., Guo, L., He, J., Yu, S., et al. (2017). Chromatin Accessibility Dynamics during iPSC Reprogramming. Cell Stem Cell *21*, 819–833 e816.

Limaye, P.B., Bowen, W.C., Orr, A., Apte, U.M., and Michalopoulos, G.K. (2010). Expression of hepatocytic- and biliary-specific transcription factors in regenerating bile ducts during hepatocyte-to-biliary epithelial cell transdifferentiation. Comp. Hepatol. *9*, 9.

Lindeman, L.C., Andersen, I.S., Reiner, A.H., Li, N., Aanes, H., Østrup, O., Winata, C., Mathavan, S., Müller, F., Aleström, P., and Collas, P. (2011). Prepatterning of developmental gene expression by modified histones before zygotic genome activation. Dev. Cell *21*, 993–1004.

Love, M.I., Huber, W., and Anders, S. (2014). Moderated estimation of fold change and dispersion for RNA-seq data with DESeq2. Genome Biol. *15*, 550.

McLean, C.Y., Bristor, D., Hiller, M., Clarke, S.L., Schaar, B.T., Lowe, C.B., Wenger, A.M., and Bejerano, G. (2010). GREAT improves functional interpretation of cis-regulatory regions. Nat. Biotechnol. *28*, 495–501.

Miyaoka, Y., Ebato, K., Kato, H., Arakawa, S., Shimizu, S., and Miyajima, A. (2012). Hypertrophy and unconventional cell division of hepatocytes underlie liver regeneration. Curr. Biol. *22*, 1166–1175.

Nashun, B., Hill, P.W., and Hajkova, P. (2015). Reprogramming of cell fate: epigenetic memory and the erasure of memories past. EMBO J. *34*, 1296–1308.

Piccolo, S., Dupont, S., and Cordenonsi, M. (2014). The biology of YAP/TAZ: hippo signaling and beyond. Physiol. Rev. *94*, 1287–1312.

Pinello, L., Xu, J., Orkin, S.H., and Yuan, G.C. (2014). Analysis of chromatin-state plasticity identifies cell-type-specific regulators of H3K27me3 patterns. Proc. Natl. Acad. Sci. USA *111*, E344–E353.

Postic, C., and Magnuson, M.A. (2000). DNA excision in liver by an albumin-Cre transgene occurs progressively with age. Genesis *26*, 149–150.

Ramírez, F., Dündar, F., Diehl, S., Grüning, B.A., and Manke, T. (2014). deepTools: a flexible platform for exploring deep-sequencing data. Nucleic Acids Res. *42*, W187–W191.

Robinson, J.T., Thorvaldsdóttir, H., Winckler, W., Guttman, M., Lander, E.S., Getz, G., and Mesirov, J.P. (2011). Integrative genomics viewer. Nat. Biotechnol. *29*, 24–26.

Sancho, R., Gruber, R., Gu, G., and Behrens, A. (2014). Loss of Fbw7 reprograms adult pancreatic ductal cells into α, δ, and β cells. Cell Stem Cell *15*, 139–153.

Schaub, J.R., Huppert, K.A., Kurial, S.N.T., Hsu, B.Y., Cast, A.E., Donnelly, B., Karns, R.A., Chen, F., Rezvani, M., Luu, H.Y., et al. (2018). De novo formation of the biliary system by TGFβ-mediated hepatocyte transdifferentiation. Nature *557*, 247–251.

Sen, P., Shah, P.P., Nativio, R., and Berger, S.L. (2016). Epigenetic Mechanisms of Longevity and Aging. Cell *166*, 822–839.

Singhal, N., Graumann, J., Wu, G., Araúzo-Bravo, M.J., Han, D.W., Greber, B., Gentile, L., Mann, M., and Schöler, H.R. (2010). Chromatin-Remodeling Components of the BAF Complex Facilitate Reprogramming. Cell *141*, 943–955.

Sirica, A.E. (1995). Ductular hepatocytes. Histol. Histopathol. *10*, 433–456.

Skibinski, A., Breindel, J.L., Prat, A., Galván, P., Smith, E., Rolfs, A., Gupta, P.B., LaBaer, J., and Kuperwasser, C. (2014). The Hippo transducer TAZ interacts with the SWI/SNF complex to regulate breast epithelial lineage commitment. Cell Rep. *6*, 1059–1072.

Soufi, A., Donahue, G., and Zaret, K.S. (2012). Facilitators and impediments of the pluripotency reprogramming factors' initial engagement with the genome. Cell *151*, 994–1004.

Stadhouders, R., Vidal, E., Serra, F., Di Stefano, B., Le Dily, F., Quilez, J., Gomez, A., Collombet, S., Berenguer, C., Cuartero, Y., et al. (2018). Transcription factors orchestrate dynamic interplay between genome topology and gene regulation during cell reprogramming. Nat. Genet. *50*, 238–249.

Stange, D.E., Koo, B.K., Huch, M., Sibbel, G., Basak, O., Lyubimova, A., Kujala, P., Bartfeld, S., Koster, J., Geahlen, J.H., et al. (2013). Differentiated Troy+ chief cells act as reserve stem cells to generate all lineages of the stomach epithelium. Cell *155*, 357–368.

Sun, X., Chuang, J.C., Kanchwala, M., Wu, L., Celen, C., Li, L., Liang, H., Zhang, S., Maples, T., Nguyen, L.H., et al. (2016). Suppression of the SWI/SNF Component Arid1a Promotes Mammalian Regeneration. Cell Stem Cell *18*, 456–466.

Takahashi, K., and Yamanaka, S. (2006). Induction of pluripotent stem cells from mouse embryonic and adult fibroblast cultures by defined factors. Cell *126*, 663–676.

Tanimizu, N., Nishikawa, Y., Ichinohe, N., Akiyama, H., and Mitaka, T. (2014). Sry HMG box protein 9-positive (Sox9+) epithelial cell adhesion molecule-negative (EpCAM-) biphenotypic cells derived from hepatocytes are involved in mouse liver regeneration. J. Biol. Chem. *289*, 7589–7598.

Tanimizu, N., Ichinohe, N., Yamamoto, M., Akiyama, H., Nishikawa, Y., and Mitaka, T. (2017). Progressive induction of hepatocyte progenitor cells in chronically injured liver. Sci. Rep. *7*, 39990.

Tarlow, B.D., Finegold, M.J., and Grompe, M. (2014a). Clonal tracing of Sox9+ liver progenitors in mouse oval cell injury. Hepatology *60*, 278–289.

Tarlow, B.D., Pelz, C., Naugler, W.E., Wakefield, L., Wilson, E.M., Finegold, M.J., and Grompe, M. (2014b). Bipotential adult liver progenitors are derived from chronically injured mature hepatocytes. Cell Stem Cell *15*, 605–618.

Tetteh, P.W., Basak, O., Farin, H.F., Wiebrands, K., Kretzschmar, K., Begthel, H., van den Born, M., Korving, J., de Sauvage, F., van Es, J.H., et al. (2016). Replacement of Lost Lgr5-Positive Stem Cells through Plasticity of Their Enterocyte-Lineage Daughters. Cell Stem Cell *18*, 203–213.

Trapnell, C., Roberts, A., Goff, L., Pertea, G., Kim, D., Kelley, D.R., Pimentel, H., Salzberg, S.L., Rinn, J.L., and Pachter, L. (2012). Differential gene and transcript expression analysis of RNA-seq experiments with TopHat and Cufflinks. Nat. Protoc. *7*, 562–578.

Wang, A., Yue, F., Li, Y., Xie, R., Harper, T., Patel, N.A., Muth, K., Palmer, J., Qiu, Y., Wang, J., et al. (2015). Epigenetic priming of enhancers predicts developmental competence of hESC-derived endodermal lineage intermediates. Cell Stem Cell *16*, 386–399.

Wells, J.M., and Watt, F.M. (2018). Diverse mechanisms for endogenous regeneration and repair in mammalian organs. Nature *557*, 322–328.

Wilson, B.G., and Roberts, C.W. (2011). SWI/SNF nucleosome remodellers and cancer. Nat. Rev. Cancer *11*, 481–492.

Xu, C.R., Cole, P.A., Meyers, D.J., Kormish, J., Dent, S., and Zaret, K.S. (2011). Chromatin "prepattern" and histone modifiers in a fate choice for liver and pancreas. Science *332*, 963–966.

Xu, J., Du, Y., and Deng, H. (2015). Direct lineage reprogramming: strategies, mechanisms, and applications. Cell Stem Cell *16*, 119–134.

Yanger, K., Zong, Y., Maggs, L.R., Shapira, S.N., Maddipati, R., Aiello, N.M., Thung, S.N., Wells, R.G., Greenbaum, L.E., and Stanger, B.Z. (2013). Robust cellular reprogramming occurs spontaneously during liver regeneration. Genes Dev. *27*, 719–724.

Yimlamai, D., Christodoulou, C., Galli, G.G., Yanger, K., Pepe-Mooney, B., Gurung, B., Shrestha, K., Cahan, P., Stanger, B.Z., and Camargo, F.D. (2014). Hippo pathway activity influences liver cell fate. Cell *157*, 1324–1338.

Zacharias, W.J., Frank, D.B., Zepp, J.A., Morley, M.P., Alkhaleel, F.A., Kong, J., Zhou, S., Cantu, E., and Morrisey, E.E. (2018). Regeneration of the lung alveolus by an evolutionarily conserved epithelial progenitor. Nature *555*, 251–255.

Zaret, K.S. (2017). Cell fate conversion: a chromatin remodeling checkpoint revealed. Cell Res. *27*, 598–599.

Zhang, Y., Liu, T., Meyer, C.A., Eeckhoute, J., Johnson, D.S., Bernstein, B.E., Nusbaum, C., Myers, R.M., Brown, M., Li, W., and Liu, X.S. (2008). Model-based analysis of ChIP-Seq (MACS). Genome Biol. *9*, R137.

Zhang, N., Bai, H., David, K.K., Dong, J., Zheng, Y., Cai, J., Giovannini, M., Liu, P., Anders, R.A., and Pan, D. (2010). The Merlin/NF2 tumor suppressor functions through the YAP oncoprotein to regulate tissue homeostasis in mammals. Dev. Cell *19*, 27–38.

STAR★METHODS

KEY RESOURCES TABLE

REAGENT or RESOURCE	SOURCE	IDENTIFIER
Antibodies		
Arid1a (1:1000, IHC/WB)	Sigma-Aldrich	Cat# HPA005456, RRID: AB_1078205
Sox9 (1:1000, IF)	Millipore	Cat#Ab5535; RRID: AB_2239761
Opn (1:1000, IF)	R and D Systems	Cat# AF808, RRID: AB_2194992
Hnf4a (1:200, IF)	Santa Cruz	Cat# sc-6556, RRID: AB_2117025
Hnf4a (1:1000, IF)	Abcam	Cat# ab181604, RRID: N/A
GFP (1:500, IF)	Santa Cruz	Cat# sc-9996, RRID: AB_627695
Fah (1:5000, IF)	Gift from Dr. Xin Wang	Cat# N/A; RRID: N/A
Ki67 (1:1000, IF/IHC)	Leica Biosystems	Cat# NCL-Ki67p, RRID: AB_442102
Yap (1:200, IF)	Santa Cruz	Cat# sc-15407, RRID: AB_2273277
Yap (1:50, ChIP)	Cell Signaling	Cat# 14074, RRID: AB_2650491
H3 (1:20,000, WB)	Abcam	Cat# ab1791, RRID: AB_302613
H2B (1:20,000, WB)	Abcam	Cat# ab1790, RRID: AB_302612
H3K27ac (2ug, ChIP)	Abcam	Cat# ab4729, RRID: AB_2118291
H3K4me1 (2ug, ChIP)	Abcam	Cat# ab8895, RRID: AB_306847
Gapdh (1:2000, WB)	Abcam	Cat# ab8245, RRID: AB_2107448
FLAG (4ug, IP/ChIP)	Sigma-Aldrich	Cat# F1804, RRID: AB_262044
FLAG (1:1000, IF)	GeneTex	Cat# GTX115043, RRID: AB_11166662
CD31 (1:200, IF)	Abcam	Cat# ab28364, RRID: AB_726362
F4/80 (1:200, IF)	Thermo Fisher Scientific	Cat# 12-4801-82, RRID :AB_465923
Desmin (1:500, IF)	Abcam	Cat# ab15200, RRID: AB_301744
CK19 (1:500, IF)	DSHB	Cat# TROMA-III, RRID: AB_213357044
RFP (1:1000, IF)	Rockland	Cat# 600-401-379, RRID: AB_2209751
Normal Rabbit IgG (2ug, ChIP)	Millipore	Cat# 12-370, RRID: AB_145841
Normal Mouse IgG (4ug, IP/ChIP)	Santa Cruz	Cat# sc-2025, RRID: AB_737182
CD24 (1:100, IF)	Santa Cruz	Cat# sc-19651, RRID: AB_626988
Hes1 (1:200, IF)	Abcam	Cat# ab71559, RRID: AB_1209570
Bacterial and Virus Strains		
AAV8.TBG.PI.Cre.rBG	University of Pennsylvania Vector Core	AV-8-PV1091
AAV8.TBG.PI.eGFP.WPRE.bGH	University of Pennsylvania Vector Core	AV-8-PV0146
AAV8.TBG.PI.FLP.rBG	University of Pennsylvania Vector Core	N/A
Chemicals, Peptides, and Recombinant Proteins		
DDC	Sigma-Aldrich	Cat# 137030
digitonin	Promega	Cat# g9411
DSG	Invitrogen	Cat# PI20593
Dynabeads	Life Technologies	Cat#10004D
SYBR® Premix Ex Taq™	Takara	Cat# rr420a
Proteinase K	Merck	Cat# 1245680100
Collagenase IV	Life Technologies	Cat# 17104019
Critical Commercial Assays		
Trueprep dna library prep kit	Vazyme Biotech	Cat# TD501
Trueprep index kit	Vazyme Biotech	Cat# TD202
MinElute PCR Purification Kit	QIAGEN	Cat# 28006
NEBNext® High-Fidelity 2X PCR Master Mix	NEB	Cat# M0541L
High Sensitivity DNA Chips	Agilent Life Sciences	Cat# 5067-4626

(*Continued on next page*)

Continued		
REAGENT or RESOURCE	SOURCE	IDENTIFIER
NEBNext Ultra DNA Library Prep Kit	NEB	Cat# E7370
VECTASTAIN Elite ABC Kit	Vector	Cat# PK6100
ApoAlert™ DNA Fragmentation Assay Kit	Clontech	Cat# 630107
Opal 4-Color Manual IHC Ki	Perkinelmer	Cat# NEL810001KT
Deposited Data		
Raw and analyzed data	This paper	GEO: GSE111502
Experimental Models: Organisms/Strains		
Mouse: *Arid1a*$^{f/f}$	Gao et al., 2008	N/A
Mouse: *Albumin-Cre*	Postic and Magnuson, 2000	N/A
Mouse: *Mx-Cre*	Kühn et al., 1995	N/A
Mouse: *Tg(Sox9-cre/ERT2)1Msan/J*	The Jackson Laboratory	Cat# JAX:018829, RRID: IMSR_JAX:018829
Mouse:*B6;129S6-Gt(ROSA)26 Sor*$^{tm9(CAG-tdTomato)Hze}$*/J*	The Jackson Laboratory	Cat# JAX:007905, RRID: IMSR_JAX:007905
Mouse:*B6;129S-Gt(ROSA)26 Sor*$^{tm65.1(CAG-tdTomato)Hze}$*/J*	The Jackson Laboratory	Cat# JAX:021875, RRID: IMSR_JAX:021875
Mouse: *Krt19*$^{tm1(cre/ERT)Ggu/J}$	The Jackson Laboratory	Cat# JAX:026925, RRID: IMSR_JAX:026925
Mouse: *Arid1a*^{3xflag}	Shanghai Biomodel Organism Co., Ltd	N/A
Mouse: *Yap*^{3xflag}	Shanghai Biomodel Organism Co., Ltd	N/A
Mouse: *B6.129(Cg)-Gt(ROSA)26 Sor*$^{tm4(ACTB-tdTomato,-EGFP)Luo}$*/J*	The Jackson Laboratory	Cat# JAX:007676, RRID: IMSR_JAX:007676
Oligonucleotides		
Primers for qPCR and ChIP-qPCR – See Table S6	This paper	N/A
Software and Algorithms		
GraphPad Prism5	GraphPad Software	Version 5.0.1
ImageJ	NIH	https://imagej.nih.gov/ij/
Bowtie2	Langmead and Salzberg, 2012	http://bowtie-bio.sourceforge.net/bowtie2/index.shtml
DeepTools v2.1.0	Ramírez et al., 2014	https://deeptools.readthedocs.io/en/develop/
MACS v1.4	Zhang et al., 2008	http://liulab.dfci.harvard.edu/MACS/
Haystack	Pinello et al., 2014	https://github.com/lucapinello/Haystack
GREAT	McLean et al., 2010	http://great.stanford.edu/public/html/
RStudio	RStudio	https://www.rstudio.com
Other		
RNA-seq data of LPLCs and hepatocytes	Tarlow et al., 2014b	GEO: GSE55552
ChIP-seq data of epigenetic factors related to liver cells – See Table S1	Cistrome Project dataset	http://cistrome.org/

LEAD CONTACT AND MATERIALS AVAILABILITY

Further requests for reagents may be directed to, and will be fulfilled by, the Lead Contact, Lijian Hui (ljhui@sibcb.ac.cn).

EXPERIMENTAL MODEL AND SUBJECT DETAILS

Mice

All mouse experiments were approved by the Institutional Animal Care and Use Committee of the Institute of Biochemistry and Cell Biology and performed in accordance with this committee's guidelines. None of the mice used in these studies had been subjected to prior procedures and were drug and test naive. Mice were housed in a temperature- and light-controlled (12-h light/dark cycle) specific pathogen-free (SPF) animal facility, in individually ventilated cages always with companion mice. Mice used in this study were 6 - 8 weeks of the age unless otherwise specified to start the mouse experiments. Both female and male mice were used for experiments, and no sex bias differences were detected in these mouse experiments.

Albumin-cre:Arid1a$^{f/f}$ (*Arid1a*$^{\Delta li}$) and *Mx1-cre:Arid1a*$^{f/f}$ (*Arid1a*$^{\Delta li^*}$) mice were generated by crossing *Arid1a*$^{f/f}$ mice (Gao et al., 2008) with *Albumin-cre* mice (Postic and Magnuson, 2000) and *Mx1-cre* mice (Kühn et al., 1995), respectively. *mTmG* (Jax 007676) mice were crossed with *Arid1a*$^{f/f}$ mice to generate *Arid1a*$^{f/f}$*:mTmG* mice. *Sox9-Cre*^{ERT2}*:RFP* mice were generated by crossing the *Sox9-Cre*^{ERT2} (Jax 018829) mice with *Rosa26-loxP-stop-loxP-RFP* (Jax 007905) mice. *Sox9-Cre*^{ERT2}*:Ai65D* were generated by crossing the *Sox9-Cre*^{ERT2} mice with *Rosa26-frt-stop-frt-loxP-stop- loxP-RFP* (Jax 021875) mice. *CK19-Cre*^{ERT2}*:RFP* mice were generated by crossing *CK19-Cre*^{ERT2} (Jax 026925) mice with *Rosa26-loxp-stop-loxp-RFP* mice. *Arid1a*^{3xflag} and *Yap*^{3xflag} mice were designed by inserting the 3x flag sequence in framed with the last exon before the stop codon of *Arid1a* and *Yap* using CRISPR/Cas9-mediated homologous recombination (Shanghai Biomodel Organism Co., Ltd). *Yap*^{3xflag} mice was further crossed with *Arid1a*$^{f/f}$ mice and *Arid1a*$^{\Delta li}$ mice to generate *Arid1a*$^{f/f}$*:Yap*^{3xflag} (*Arid1a-WT:Yap*^{3xflag}) and *Arid1a*$^{\Delta li}$*:Yap*^{3xflag} (*Arid1a-KO:Yap*^{3xflag}) mice. *Arid1a*$^{\Delta li}$, *Arid1a*$^{\Delta li^*}$ *Arid1a-WT:Yap*^{3xflag} and *Arid1a-KO:Yap*^{3xflag}, *mTmG, Arid1a*$^{f/f}$*:mTmG, Sox9-Cre*^{ERT2}*:RFP*, *Sox9-Cre*^{ERT2}*:Ai65D* and *CK19-Cre*^{ERT2}*:RFP* mice were maintained on a mixed background (C57BL/6J and 129S6/SvEvTac). *Arid1a*^{3xflag}, *Yap*^{3xflag} and *Yap*$^{f/f}$ (Zhang et al., 2010) mice were maintained on C57BL/6J background.

To induce liver injury, mice were given 0.1% DDC (Sigma-Aldrich) diet (0.1g per 100 g) for 3 days to 8 weeks. For the DAPM model, mice received one intraperitoneal injection of DAPM at a dose of 100mg/kg body weight and were euthanized after 5 days. For bile duct ligation (BDL) injury, the hepatic duct was ligated, and mice were euthanized 2 weeks later.

Lineage tracing of liver progenitor-like cells and HybHP in DDC-induced periportal liver regeneration

To investigate the contribution of Hnf4a$^+$Sox9$^+$ cells to liver regeneration, *Sox9-Cre*^{ERT2}*:Ai65D* mice were treated with 2.5x10^{11} genomic particles of AAV2/8-TBG-Flp (AAV-Flp) in the resting condition. After 2 weeks virus washing out, these mice received DDC treatment for 2 weeks and were administrated with 150mg/kg tamoxifen every 3 days for 4 times. After 2 weeks DDC injury, these mice were then kept on normal diet for 8 weeks.

To label the HybHP cells, the *Sox9-Cre*^{ERT2}*:RFP* mice were administrated with 150mg/kg tamoxifen every 3 days for 4 times. Two weeks after tamoxifen treatment, *Sox9-Cre*^{ERT2}*:RFP* mice were kept with DDC for 2 weeks and then recovered for 8 weeks. The contribution of LPLCs and HybHP in DDC-induced periportal liver regeneration were analyzed after the recovery.

METHOD DETAILS

AAV virus *in vivo* delivery

For AAV virus infection, 2.5x10^{11} genomic particles of AAV-GFP, AAV-Cre and AAV-Flp (purchased from University of Pennsylvania Vector Core) were reconstituted in 200ul PBS injected intravenously through tail veil injection with BD Ultra-Fine Insulin Syringes.

Hydrodynamic tail-vein injection

For sleeping beauty transposon cloning, constitute active YapS127A was cloned into the transposon vector. A sterile 0.9% NaCl solution/plasmid mix per mice was prepared containing 10 ug DNA of each transposon vector together with 1.8 ug CMV-SB13 transposase. Mice with body weight ranging from 18 - 20 g were injected with the 0.9% NaCl solution/plasmid mix into the lateral tail vein with a total volume corresponding to 10% of body weight in 5-7 s.

Histology, immunohistochemistry and immunofluorescence

For paraffin sections, liver samples were fixed overnight in 4% PFA (4°C) and embedded in paraffin blocks. For making frozen sections, liver were perfused with PBS through the portal vein and fixed 30min in 4% PFA (4°C), followed by cryopreserved in 30% sucrose overnight (4°C) prior to freezing in OCT tissue blocks. Immunohistochemistry staining and hematoxylin and eosin staining were performed as previously described (Li et al., 2016). For immunofluorescence, paraffin sections (3 um) or frozen sections (8 um) were washed 2 × 15 min in PBS, permeabilized in 0.2%–0.5% Triton X-100 and blocked in 5% normal donkey serum for 1 hours and stained with primary antibody for overnight, Primary antibody were detected using fluorescent-conjected second antibodies (Jackson Lab). Sections were stained with DAPI (4',6-Diamidino-2-Phenylindole) and mounted with fluorescence mounting medium (Dako). For the antibodies from the same species, Opal^{TM} 4-Color Manual IHC Kit (PerkinElmer) was used on FFPE liver sections according to the manufacturer's protocol. Images were taken using an Olympus BX51 microscope. Primary antibodies and dilution factor were listed on Key Resources Table.

Immunoblot analysis

For nuclear and cytoplasm protein isolation, cells were suspended in Buffer A (10 mM HEPES pH7.9, 1.5 mM MgCl2, 10 mM KCl, 0.5 mM DTT) supplemented with protease inhibitor cocktail (Sigma) on ice for 15 min. NP40 was then added into a final concentration of 0.25% followed by vortex for 20 s. After centrifugation at 4 000 rpm for 5 min, cells supernatants were served as cytoplasm proteins, and cell pellets were collected as nucleus. Nucleus proteins were further extracted in Buffer C (20mM HEPES pH7.9, 25% glycerol, 0.42M NaCl, 1.5mM MgCl2, 0.2mM EDTA, and 0.5mM DTT) supplemented with protease inhibitor cocktail (Sigma) on ice for 1h with vortex every 10min. For immunoblot analysis, proteins were separated by SDS-PAGE, and transferred to a PVDF membrane (Millipore). The membrane was blocked with 5% (w/v) reagent-grade nonfat milk (Cell Signaling Technology) and incubated with primary antibodies (see Key Resources Table) at 4°C to overnight, followed by secondary antibody incubation. The protein bands were visualized using ClarityTM Western ECL substrate (Bio-Rad).

RNA-seq

Total RNA were extracted from *Arid1a-WT* and *Arid1a-KO* livers using Trizol (Invitrogen) according to the manufacturer's instructions. Sequencing library was prepared from one microgram of total RNA using Illumina TruSeq RNA Sample Prep Kit. Paired-end 150 bp read length sequencing was performed on Illumina Hiseq 4000 sequencer.

ATAC-seq

ATAC-seq were performed as described before (Buenrostro et al., 2015; Corces et al., 2017). Nuclei isolated from 20,000 counted cells were used for transposition reaction with transposase (Vazyme Biotech). Column-purified DNA was amplified in 50 ul reactions with high-fidelity 2X PCR Master Mix (New England Biolabs) using primers with unique barcodes (Vazyme Biotech) to setup library. Library was sequenced using Illumina HiSeq X Ten sequencer by Annoroad Gene Tech. Co., Ltd. to obtain 150bp paired-end reads.

Arid1a-WT and *Arid1a-KO* hepatocytes were isolated from normal and DDC-injured mouse livers by a two-step liver collagenase perfusion. Perfused hepatocytes were filtered through a 70um filter (BD Bioscience) and were further purified by a series of low speed gravity centrifugation (3 × 2min x 50 g) as previously described (Tarlow et al., 2014a). For the isolation of LPLCs, a low dosage tamoxifen (50mg/kg), which did not label hepatocytes in normal mouse livers (Tarlow et al., 2014a), was given to the 2 weeks DDC-injured *Sox9-Cre^{ERT2}:RFP* reporter mice by intraperitoneal injection. The DDC-injured hepatocytes were isolated 2 days later after tamoxifen injection via liver perfusion and gravity purification (3 × 2min x 50 g). The Sox9^{+} LPLCs were further isolated by sorting the RFP^{+} hepatocytes by the BD influx cell sorter based on size/granularity and RFP expression. For isolating of bile duct cells, the *CK19-Cre^{ERT2}:RFP* reporter mice were treated with 3 individual oral gavage of tamoxifen (150mg/kg) under resting condition. Non parenchymal cells (NPCs) were isolated 2 weeks later as previous reported (Dorrell et al., 2008). The bile duct cells were further isolated by sorting RFP^{+} NPCs in the BD influx cell sorter based on size/granularity and RFP expression.

ChIP-seq and ChIP-qPCR

Hepatocytes were isolated from mouse livers by two-step liver collagenase perfusion and gravity purification (3 × 2min x 50 g). For ChIP assay of histone modifications in *Arid1a-WT* and *Arid1a-KO* hepatocytes, 1x10^{7} cells were cross linked by 1% formaldehyde for 10 min, followed by glycine quenching for 5 min. For ChIP assay of FLAG in *Arid1a^{3xlfag}* hepatocytes, 1x10^{7} cells were cross linked by 1% formaldehyde for 15 min, followed by glycine quenching for 5 min. For ChIP assay of Yap in injured-*Arid1a-WT* and -*Arid1a-KO* hepatocytes, 1x10^{7} cells were dual-cross-linked with 2 mM disuccinimidyl glutarate (DSG; Invitrogen, 20593) for 30 min and 1% formaldehyde for 15 min, followed by glycine quenching for 5 min. After three time washes in PBS, nuclear extracts were further generated. Chromatin was fragmented using Covaris sonication. The following antibodies were used for immunoprecipitation solubilized chromatin: H3K27ac, H3K4me1, Yap, FLAG, normal rabbit IgG, and normal mouse IgG at 4°C overnight (see Key Resources Table). Antibody chromatin complexes were pulled down with Protein G Dynabeads (Life Technologies, 10004D), washed and eluted. Chromatin cross-links were reversed, and samples were treated with proteinase K and RNase A. Input and ChIP DNA was extracted with the MinElute PCR purification kit (QIAGEN) and quantified with the Qubit (Life Technologies). For ChIP-seq, purified ChIP DNA was used to prepare sequencing libraries via NEBNext Ultra DNA Library Prep Kit for the Illumina (E7370) and sequenced on Illumina HiSeq X Ten sequencer to obtain 150bp paired-end reads. Primers for validation sites by ChIP-qPCR were included in Table S6.

QUANTIFICATION AND STATISTICAL ANALYSIS

RNA-seq analysis

All sequencing reads from RNA-seq were trimmed by Trim Galore to improve mapping efficiency and reduce the chance of misalignments. Trimmed reads were aligned to the mouse genome (Mm10, Genome Reference Consortium GRCm38) using TopHat v2.0.6 (Trapnell et al., 2012). FPKM (fragments per kilobase of exon per million fragments mapped) values were calculated by Cufflinks using default parameters for gene expression levels. Differential expression was defined using the indicated fold-changes and false discovery rate (FDR) 0.05 by DEseq2 (Love et al., 2014). Gene Set Enrichment Analysis (GSEA) (http://software.broadinstitute.org/gsea/index.jsp) was used to identify gene sets and pathways associated with gene expression data. For published data analysis in Table S2, RNA-seq data for hepatocytes and LPLCs were retrieved from published RNA-seq data (GEO: GSE55552) (Tarlow et al., 2014b). Genes altered in hepatocyte to LPLC conversion were identified by differential gene expression between hepatocytes and LPLCs (rpkm > 1, fold change > 1.5, q < 0.05). Genes with 1.5-fold increase of expression in LPLCs were further identified as LPLC-enriched genes. Hepatocyte to LPLC conversion-related pathways were retrieved from Tarlow et al. (Tarlow et al., 2014b).

ATAC-seq analysis

All sequencing reads from ATAC-seq were trimmed by Trim Galore to improve mapping efficiency and reduce the chance of misalignments. Trimmed reads were aligned to the mouse genome (Mm10, Genome Reference Consortium GRCm38) using Bowtie2 (Langmead and Salzberg, 2012). Reads on autosomes excluding the ENCODE mouse blacklisted regions were kept for downstream analysis and duplicate reads were removed using DeepTools v2.1.0 (Ramírez et al., 2014). Peaks were identified using MACS v1.4 (Zhang et al., 2008) with the p value cut-off 10^{-5}. Independent biological replicates showed a high degree of similarity (Pearson correlation coefficient, r = 0.9952-0.9999), so the replicate data were subsequently combined and processed. ATAC-seq signal tracks were presented by Integrative Genomics Viewer (IGV) software (Robinson et al., 2011), and profiles were generated by DeepTools.

To compare hepatocytes chromatin accessibility under the resting condition and DDC treatment, ATAC-seq signals were first normalized by computing the number of reads per kilobase of bin per million reads sequenced (RPKM). To minimize the batch and cell type variation, the RPKM values were further quantile-normalized using Haystack (Pinello et al., 2014), with 50-bp windows. For the genomic distribution of ATAC peaks, promoters regions were identified by HOMER v4.10 (Heinz et al., 2010). The remaining peaks that only overlapped with H3K4me1 or both with H3K4me1 and H3K27ac were identified as H3K4me1^{+} enhancers and H3K4me1^{+}H3K27ac^{+} enhancers, respectively.

For identification of ATAC peaks associated genes, nearby genes and enriched pathways were identified via GREAT (McLean et al., 2010) using basal plus extension with default parameters. Ontologies of genes were identified by R clusterProfiler v3.4.0. Motifs enriched in ATAC-seq peaks were identified using HOMER *de novo* algorithm v4.10 (Heinz et al., 2010) based on the cumulative binomial distribution.

ChIP-seq analysis

All sequencing reads were aligned to the mouse genome (Mm10, Genome Reference Consortium GRCm38), using Bowtie2 (Langmead and Salzberg, 2012). Peaks calling, and visualization were generated as described for ATAC-seq.

For binding significance of epigenetic factors on hepatocyte to LPLC conversion altered genes (Table S1), the ChIP-seq data were retrieved from public Cistrome Project dataset with biological sources related to livers and hepatocytes (http://cistrome.org/). The epigenetic factors bound genes were identified by GREAT (McLean et al., 2010) using the parameters basal plus extension, 5kb upstream and 1kb downstream of TSS without distal extension. Identified epigenetic factors bound genes were overlapped with hepatocyte to LPLC conversion altered genes (see RNA-seq analysis), and the binding significances were calculated by Chi-square test.

Statistical Analysis

All data are presented as the mean ± SEM "n" represented the number of biological replicates and animals and were indicated in the figures or figure legends. For quantification of sections, three to five random periportal fields of each liver samples unless otherwise specified were imaged and then quantified using ImageJ. No statistical method was used to predetermine sample size. All siblings with indicated genotypes were used in this study without randomization. Sample processing was not blinded. For statistic evaluation, an unpaired two-side Student's t test was performed using Graphpad Prism 5 software and mentioned in the figure legends. To compare the overlap of the two cluster genes or peaks, significance was assessed by Chi-square test using the R package (stats 3.5.1, function:chisq.test()) and mentioned in the figures. The significance was set when P was < 0.05.

DATA AND CODE AVAILABILITY

Data Resources

All the RNA-seq, ATAC-seq, and ChIP-seq data are available under GEO accession GEO: GSE111502.